Diversity of Early Kilonova with the Realistic Opacities of Highly Ionized Heavy Elements

Smaranika Banerjee[1,2] , Masaomi Tanaka[1,3] , Daiji Kato[4,5] , and Gediminas Gaigalas[6]
[1] Astronomical Institute, Tohoku University, Aoba, Sendai 980-8578, Japan; smaranika.banerjee@astro.su.se
[2] Stockholm University, Roslagstullsbacken 21, 114 21 Stockholm, Sweden
[3] Division for the Establishment of Frontier Sciences, Organization for Advanced Studies, Tohoku University, Sendai 980-8577, Japan
[4] National Institute for Fusion Science, National Institutes of Natural Sciences, Oroshi-cho, Toki, Gifu 509-5292, Japan
[5] Interdisciplinary Graduate School of Engineering Sciences, Kyushu University, Kasuga, Fukuoka 816-8580, Japan
[6] Institute of Theoretical Physics and Astronomy, Vilnius University, Saulėtekio av. 3, LT-10257 Vilnius, Lithuania

Abstract

We investigate early ($t < 1$ day) kilonova from a neutron star merger by deriving atomic opacities for all the elements from La to Ra ($Z = 57$–88) ionized to the states V–XI. The opacities at high temperatures for the elements with open f-shells (e.g., lanthanides) are exceptionally high, reaching $\kappa_{\exp} \sim 3 \times 10^3 \, \mathrm{cm^2 \, g^{-1}}$ at $\lambda \leqslant 1000 \, \text{Å}$ at $T \sim 70{,}000$ K, whereas the opacities at the same temperature and wavelengths for the elements with open d-, p-, and s-shells reach $\kappa_{\exp} \sim 1$, 0.1, and $0.01 \, \mathrm{cm^2 \, g^{-1}}$, respectively. Using the new opacity data set, we derive early kilonovae for various compositions and density structures expected for neutron star merger ejecta. The bolometric luminosity of the lanthanide-rich ejecta shows distinct signatures and is fainter than that of the lanthanide-free ejecta. Early luminosity is suppressed by the presence of a thin outer layer, agreeing with the results of Kasen et al. and Banerjee et al. The early brightness in the Swift UVOT filters and in the optical g, r, i, and z filters for a source at 100 Mpc are about $\sim$22–19.5 and $\sim$21–20 mag, respectively, at $t \sim 0.1$ day. Such kilonovae are ideal targets for the upcoming UV satellites, such as ULTRASAT, UVEX, and DORADO, and the upcoming surveys, e.g., the Vera Rubin Observatory. We suggest that the gray opacities that reproduce the bolometric light curves with and without lanthanides are $\sim$1–10 and $\sim$0.8 $\mathrm{cm^2 \, g^{-1}}$.

Unified Astronomy Thesaurus concepts: Neutron stars (1108); Nucleosynthesis (1131); R-process (1324); Stellar atmospheric opacity (1585); Radiative transfer (1335); Gravitational waves (678)

Supporting material: machine-readable table

1. Introduction

Binary neutron star mergers have long been hypothesized to be one of the most plausible sites for heavy element synthesis. In the neutron-rich material ejected after a neutron star merger, heavy ($Z > 26$) elements are synthesized via rapid neutron capture (r-process, e.g., Lattimer & Schramm 1974; Eichler et al. 1989; Freiburghaus et al. 1999; Korobkin et al. 2012; Wanajo et al. 2014). Radioactive decay of freshly synthesized heavy elements produces a transient in the ultraviolet-optical-infrared (UVOIR) range, called a kilonova (e.g., Li & Paczyński 1998; Kulkarni 2005; Metzger et al. 2010). The recent detection of the kilonova AT2017gfo from the neutron star merger (e.g., Coulter et al. 2017; Valenti et al. 2017; Yang et al. 2017) by the follow-up observation of the gravitational wave signal GW170817 (Abbott et al. 2017) has considerably progressed our understanding of the origin of heavy elements.

Several efforts have been made to model the kilonova AT2017gfo, which evolved from UV and optical to near-infrared in the timescale of about a week (e.g., Coulter et al. 2017; Cowperthwaite et al. 2017; Drout et al. 2017; Smartt et al. 2017; Utsumi et al. 2017; Valenti et al. 2017; Yang et al. 2017). The light curves at late times ($t > 1$ day, hereafter t denotes the time after the merger) are well explained by the radioactive decay of the heavy elements or kilonova (e.g.,

Kasen et al. 2017; Perego et al. 2017; Shibata et al. 2017; Tanaka et al. 2017; Kawaguchi et al. 2018; Rosswog et al. 2018). Nonetheless, the source of the emission at early time ($t < 1$ day) had been a matter of debate (see Arcavi 2018) since it was not clear the radioactive heating is enough to explain whether the early kilonova (e.g., Villar et al. 2017; Waxman et al. 2018). It may require other heating sources, such as the cooling from the shocked ejecta formed by the jet–ejecta interaction (e.g., Kasliwal et al. 2017; Piro & Kollmeier 2018; Hamidani & Ioka 2023a, 2023b; Hamidani et al. 2024) or β decays of free neutrons (Metzger et al. 2015; Gottlieb & Loeb 2020) or central engine activity (e.g., Metzger et al. 2008, 2018; Yu et al. 2013; Metzger & Fernández 2014, Metzger et al. 2018). Also, some recent studies showed (or demonstrated) that kilonova powered by radioactive heating can naturally explain the early light curve (e.g., Banerjee et al. 2020; Klion et al. 2021).

Kilonova light curves strongly depend on the bound–bound opacity of the r-process elements, which requires their atomic data (e.g., Kasen et al. 2013; Tanaka & Hotokezaka 2013; Fontes et al. 2015, 2020; Wollaeger et al. 2017; Tanaka et al. 2018; Tanaka et al. 2020). However, such atomic data have largely been unavailable (see Kramida et al. 2020). In the past decade, calculations of atomic opacity have been the intense focus of research (e.g., Kasen et al. 2013; Tanaka & Hotokezaka 2013; Fontes et al. 2015, 2020, 2023; Wollaeger et al. 2017; Tanaka et al. 2018, 2020; Gaigalas et al. 2019; Rynkun et al. 2022; Flörs et al. 2023), although all of these studies focused on the relatively lower ionized elements, with a

maximum up to the third level (or IV in spectroscopic notation; hereafter used to describe the ionization), which are important for the kilonova at late times ($t > 1$ day).

The atomic opacity at early time ($t < 1$ day) is determined by the highly ionized heavy elements since the neutron star merger ejecta are highly ionized at early time. For the AT2017gfo-like binary neutron star merger with an ejecta mass of $M_{\rm ej} \sim 0.05\,M_\odot$ (Kasen et al. 2017; Kasliwal et al. 2017; Waxman et al. 2018; Banerjee et al. 2020), moving with an average velocity of $v_{\rm avg} \sim 0.1c$ (e.g., Tanaka et al. 2017), the maximum ionization at around $t \sim 0.1$ day is $\sim$XI, owing to the high temperature of ejecta of $T \sim 10^5$ K (Banerjee et al. 2020; Klion et al. 2021). Atomic opacity calculations for the highly ionized (V–XI) elements have been started relatively recently (e.g., Banerjee et al. 2020, 2022). However, the calculations are limited to the lighter r-process elements (Ca–Ba, $Z = 20$–56, Banerjee et al. 2020) and selected rare earth elements ($Z = 57$–71), lanthanides (see Banerjee et al. 2022 for atomic opacities of Nd, $Z = 60$; Sm, $Z = 62$; and Eu, $Z = 63$; also see Carvajal Gallego et al. 2022a, 2022b, 2023 for the atomic opacities for La–Sm, $Z = 57$–61, ionized to states V–X; Maison et al. 2022 for Lu ionized to V). The atomic opacity for many of the lanthanides, such as the lanthanides with $Z = 64$–71, and the post-lanthanide r-process elements ($Z > 71$, e.g., Wanajo et al. 2014) have yet to be included.

Calculation of the atomic opacity for all the elements is required to understand kilonova from different viewing angles. This is because, in neutron star mergers, different elements are inhomogeneously distributed (see Shibata & Hotokezaka 2019), which introduces angle dependence in light curves due to the different opacities for different elements. For example, if lanthanides are present in the ejecta, it causes the opacity to increase dramatically (e.g., Kasen et al. 2013; Tanaka et al. 2018, 2020; Fontes et al. 2020), affecting the light curves. Such lanthanides (also the heavy r-process elements $Z > 71$) are expected to be mainly distributed in the equatorial region by dynamical mass ejection. On the other hand, the lighter r-process elements ($Z \leqslant 56$) are expected to be distributed in the shocked dynamical ejecta in the polar direction or in the relatively isotropic outflow from the accretion disk (e.g., Bauswein et al. 2013; Fernandez & Metzger 2014; Metzger & Fernández 2014; Perego et al. 2014; Just et al. 2015, 2022; Sekiguchi et al. 2015; Lippuner et al. 2017; Fujibayashi et al. 2018, 2020a, 2020b; Miller et al. 2019).

Understanding the kilonova from different directions starting from early time is important to extract the abundances from observations. The fourth gravitational wave observing run (O4), which started in 2023, is expected to make several joint detections of gravitational waves and kilonova per calendar year (e.g., Colombo et al. 2022). The detected events might have viewing angles different from each other. Hence, calculations of the atomic opacity suitable to calculate the light curve from early time are necessary.

In this paper, we perform the first systematic atomic opacity calculation for all the heavy r-process elements, including lanthanides (La–Ra, $Z = 57$–88) ionized to the states V–XI. This work, together with that of Banerjee et al. (2020, 2022), provides the atomic opacity suitable for early time for all the r-process elements Ca–Ra ($Z = 20$–88). We show our new atomic and opacity calculations in Section 2. Using the new opacity data set, we study the early kilonova emission at $t < 1$ day. The radiative transfer simulations performed for such

purpose are discussed in Section 3. Since now we have the complete atomic opacity to calculate the light curves for all possible compositions, we assess the applicability of the gray approximations used in many previous studies for modeling the early kilonova (e.g., Villar et al. 2017) in Section 4. Finally, we provide our conclusions in Section 5. Note that the AB magnitude system is adopted throughout the article.

2. Opacity for Neutron Star Merger

In this section, we discuss the bound–bound opacity calculation for the neutron star merger ejecta. In the case of supernovae and neutron star mergers, the matter is expanding with a high velocity and a high-velocity gradient. In this case, the photons are continuously redshifted in the comoving frame, and the redshifted photons progressively interact with lines. Note that the lines are not infinitely sharp, but are broadened due to the different mechanisms (mainly due to the thermal motion in neutron star merger ejecta). If the lines do not overlap with each other, i.e., if the interaction of the photons with different lines is independent of each other, then the average contribution from multiple lines within a chosen wavelength bin is defined to be the opacity (Karp et al. 1977; Eastman & Pinto 1993). This is called the expansion opacity (Sobolev 1960), calculated as

$$\kappa_{\rm exp}(\lambda) = \frac{1}{\rho c t} \sum_l \frac{\lambda_l}{\Delta \lambda}(1 - e^{-\tau_l}), \qquad (1)$$

where λ_l is the transition wavelength in the wavelength interval of $\Delta \lambda$ and τ_l is the Sobolev optical depth at the transition wavelength, calculated as

$$\tau_l = \frac{\pi e^2}{m_e c} n_l \lambda_l f_l t. \qquad (2)$$

Here, n_l is the number density of the lower level of the transition, and f_l is the strength of the transition. The number density at the lower level of the transition is evaluated by the Boltzmann distribution:

$$n_l = \frac{g_l}{U(T)} \exp(-E_l/kT), \qquad (3)$$

where g_l and E_l are the statistical weight and the excited energy of the lower level, respectively, and $U(T)$ is the partition function of the ion. Although the partition function is temperature dependent, it can be approximated as a temperature-independent quantity for a certain temperature range of interest. When the temperature is low as compared with the typical energy scale of the excited states, i.e., the population in the higher energy levels is negligible, the partition function can be estimated by summing the well-populated low-lying energy levels such as $U(T) \sim \sum_{k=0}^{E_{\rm th}} g_k e^{-E_k/k_B T} \sim \sum_{k=0}^{E_{\rm th}} g_k$. Such a simplification has been used in some previous works (e.g., Banerjee et al. 2020; Tanaka et al. 2020; Banerjee et al. 2022).[7] However, this assumption can affect the opacities at high temperatures, especially in the case of the lanthanides due to their dense energy level structure (as also mentioned in

---

[7] In Equation (4) of Tanaka & Hotokezaka (2013) and Equation (7) of Gaigalas et al. (2019), the simplified partition function was denoted as g_0 (the usual notation for the statistical weight of the ground state), but actually $\sum_{k=0}^{E_{\rm th}} g_k$ was adopted by adding the statistical weights for the levels with the same LS term to the ground level.

Carvajal Gallego et al. 2023).[8] Hence, in this study, for the complete systematic opacities for the highly ionized elements, we use the temperature-dependent partition function considering all the energy levels. For a more detailed discussion on the effect of the choice of partition function on opacity, see Appendix A.

Note that the opacity is calculated by assuming local thermodynamic equilibrium (LTE). Hence, to calculate the ionization fraction, we solve the Saha ionization equation, and we determine the population of the excited levels via Boltzmann statistics. The assumption of LTE is invalid if the nonthermal processes significantly affect the ionization and excitation structure. However, Banerjee et al. (2022) estimate that at early times ($t < 1$ day), the effect of the nonthermal processes on the ionization/excitation is not significant. Hence, we adopt the LTE assumption in this paper.

It is evident from Equations (1) and (2) that the calculation of the expansion opacity requires atomic data (e.g., energy levels, transition wavelengths, strength of transitions). Hence, we first perform the atomic structure calculation for the elements La–Ra ($Z = 57$–88) with the ionization states of V–XI as discussed in the next section.

2.1. Atomic Structure Calculations

We perform atomic structure calculations by using the Hebrew University Lawrence Livermore Atomic Code (HUL-LAC; Bar-Shalom et al. 2001). HULLAC uses zeroth-order solutions of single-particle Dirac equations with a parametric central field potential as a basis for relativistic configuration interaction calculations. The central field represents the combined effect of the nuclear field and the spherically averaged electron–electron interaction. Parameters of the central field are optimized so that the first-order configuration averaged energies of the ground, and low-lying excited states are minimized. The many-electron wave function is constructed from the antisymmetrized products of the orbitals in the j–j coupling scheme. Breit interaction and quantum electrodynamic correction are also taken into account. More details on the HULLAC calculations for heavy elements can be found in previous studies (e.g., Tanaka et al. 2018; Banerjee et al. 2022; Rynkun et al. 2022).

Note that HULLAC uses the parametric central field potential constructed from the electron distribution of the slater type orbital, for which the ground state configuration of the next ion state is used. Hence, knowledge of the ground configurations is required to perform atomic calculations. However, for highly ionized atoms, the ground configurations are not well established for several elements. This problem is especially severe in the case of highly ionized lanthanides ($Z = 57$–71). For example, the ground states for the highly ionized lanthanides provided by the NIST Atomic Spectra Database (ASD; Kramida et al. 2020) are based on approximated and simplified theoretical calculations (Carlson et al. 1970; Sugar & Kaufman 1975; Martin et al. 1978; Rodrigues et al. 2004). The use of such ground states can be a source of

uncertainty in the atomic opacity. Hence, it is important to use the correct ground configurations to calculate the opacity.

We estimate the ground configurations of the highly ionized lanthanides (V–XI) by using the method originally devised by Banerjee et al. (2022) to derive the ground configurations of the three lanthanides (Nd, $Z = 60$; Sm, $Z = 62$; Eu, $Z = 63$) ionized up to XI. We extend the calculation to all the lanthanides. We perform several atomic structure calculations by systematically varying the central potential. For designing the central potential, (1) we consider different electron distribution in the $4f$ and $5p$ shells (the two open shells in the highly ionized lanthanides, Kramida et al. 2020) and (2) optimize the central field potential with different sets of configurations. For each case, we identify the ground configuration as the one that generates the configuration state function with the largest mixing coefficient for the lowest energy level. If the same configuration is identified as the ground state for all the different calculations, we take that as the ground configuration of that ion. More details on this method can be found in Banerjee et al. (2022).

A comparison of our results for ground states for lanthanides ionized to V–XI with those in the NIST ASD shows that our results are mostly different from the simplified calculations provided in NIST ASD (mainly the work by Carlson et al. 1970). This has already been discussed by Banerjee et al. (2022) for the selected lanthanides (Nd, Sm, Eu). This is because of the fact that Carlson et al. (1970) remove the consecutive electron from the least bound orbitals determined from the solution of the relativistic Hartree–Fock wave function for the neutral atoms to provide the ground configuration. Our work, on the contrary, calculates atomic energy levels for individual ions with an effective central field potential by taking electron–electron interaction into account.

We also compare our results with the works by Cowan (1973) and Cowan (1981), which provide the ground configurations of Nd, Gd, and Er for the ionization states of V–X. These works have performed the atomic calculations for each ion, unlike Carlson et al. (1970), although their method is approximated by the use of the Hartree-plus-statistical exchange, the so-called HX method (Cowan 1967), which considers the approximated relativistic correction. Our result from HULLAC mostly agrees with the results in Cowan (1973, 1981), although the agreement is not perfect (the results do not agree for the ions Nd X, Gd VII, Gd VIII, Er X). This is likely due to the fact that only the first-order relativistic effect is taken into account in the works by Cowan (1973) and Cowan (1981).

We also compare our results with another more recent systematic study by Kilbane & O'Sullivan (2010). They perform ab initio calculations using the Hartree–Fock approximation with the relativistic and correlation corrections mode of the Cowan suite of atomic codes (Cowan 1981), and they choose the ground state configuration as the one with the lowest calculated average energy. Our results have good agreement for the ions V, VI, VII (except for the ions of Pm to Dy), IX (except for the ions of Gd to Dy), and X (except for the ions of Ho to Tm). However, our results have relatively poor agreement with the ions VIII (does not match for Nd to Dy, Tm, Yb) and XI (does not match for Pr to Tb, Ho to Lu).

We use the derived ground configurations for the highly ionized lanthanides for the atomic structure calculations for opacity, as these are more realistic ground configurations than
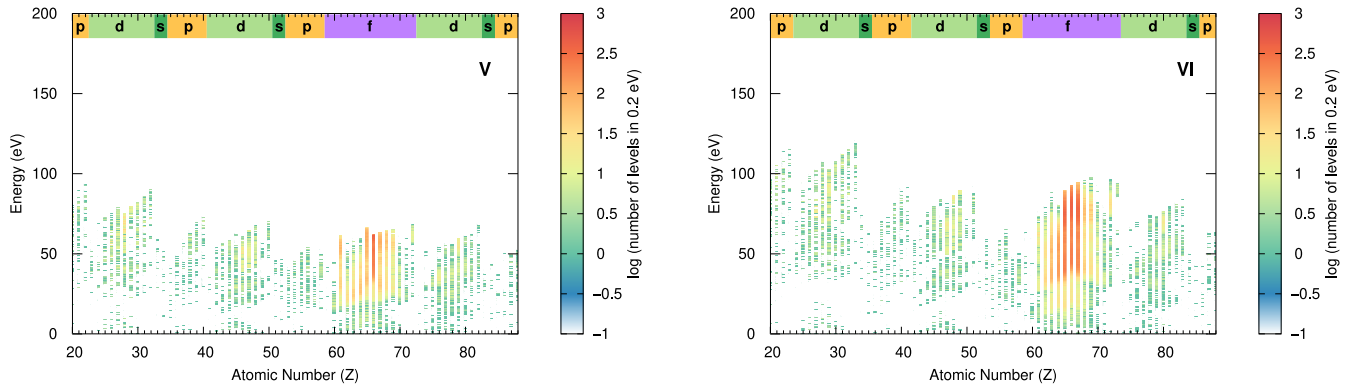

Figure 1. The energy level density distribution for all elements with the ionization states of V (left) and VI (right). Only the energy levels below the ionization threshold are included. The colored boxes on the top indicate the valence shells in different ions.

the previous works based on different approximated schemes (e.g., Carlson et al. 1970). For the post-lanthanides (elements with atomic number $Z = 72$–88), we use the ground states provided in the NIST ASD (Kramida et al. 2020), following previous works (e.g., Kasen et al. 2013; Banerjee et al. 2020; Tanaka et al. 2020). Here, we want to stress that the choice of the ground states affects the opacity calculation, and the comparison of opacity using ground states from different calculations (e.g., Kilbane & O'Sullivan 2010) is interesting and within the scope of future work.

We calculate the excited levels for opacity by including several configurations together with the ground one. Note that the choice of configurations limits the completeness of the atomic data (e.g., the number of transitions), and hence, affects the opacity. Therefore, it is important to assess whether the configurations included are sufficient to determine the opacity. For this purpose, we perform the convergence test for the few lanthanide ions (Nd, Sm, Eu, at the ionization state of IX) in our previous work (see Banerjee et al. 2022) to understand which orbitals are contributing toward the important transitions for the opacity. In this paper, the choice of the configurations is motivated by that work. We show all the configurations used in our work in Table B1, where the first configuration always represents the ground one. All the configurations used for optimization of the central potential are marked in bold in Table B1.

2.2. Energy Levels and Transitions

Figures 1 and 2 show the energy level distribution obtained from our atomic structure calculations. We also include the lighter r-process elements ($Z = 20$–56, Banerjee et al. 2020) and the three lanthanides (Nd, Sm, Eu) already discussed in Banerjee et al. (2022) for comparison. Note that the number of energy levels below the ionization threshold is shown since these are the only levels that are relevant for the bound–bound opacity. The color scale represents the level density in the 0.2 eV energy bin. The colored boxes on the top of the figure indicate the valence electron shell of the individual ions.

Note that the valence electron shells in highly ionized states are different than the valence shells in neutral atoms. For example, Pb ($Z = 82$), a p-group element in a neutral state, has a d-shell as the outermost orbital in the ionization state of IX (Table B1). Again, Hf ($Z = 73$), which is a d-shell element in a neutral state, has an f-shell as a valence shell at higher ionization ($>$V, Table B1). Depending on the valence shell, the energy level distribution of a particular ion might show a

completely different trend than its neutral or lower ionization state.

The energy level density in the highly ionized elements is the maximum when f-shell electrons are present. For instance, the energy level density is extremely high for the elements Pr–Ta ($Z = 59$–73), which have an open f-shell as the valence shell for ionization states of V–XI. This is due to the large number of available states when an open f-shell is present. This behavior for the elements with f-shell is well known for the low-ionization cases ($Z = 57$–71, e.g., see Kasen et al. 2013; Tanaka & Hotokezaka 2013; Fontes et al. 2015, 2020, 2023; Wollaeger et al. 2017; Tanaka et al. 2018, 2020). However, the energy level density for the elements with an open f-shell at higher ionization is even higher. This is because at higher ionization, the elements with an open f-shell also possess an open p-shell (Table B1), increasing the total number of the available states (or complexity) for the electrons. The high density of the energy levels for the highly ionized lanthanides is also observed by Banerjee et al. (2022) for Nd ($Z = 60$), Sm ($Z = 62$), and Eu ($Z = 63$). Now, the overall trend for highly ionized lanthanides is clearer with the extension of the calculations to all the lanthanides.

For the other elements, the energy level density is the maximum for the elements with an open d-shell, followed by the elements with open p- and s-shells (Figures 1 and 2). For example, at the ionization state of IX, the density of energy levels appear in decreasing order for the elements that possess an open d-shell (Ir–Rn, $Z = 77$–86), an open p-shell without an f-shell (W–Os, $Z = 74$–76), and an open s-shell (Fr–Ra, $Z = 87$–88; Figure 2). Note that similar trends are followed for the lighter r-process elements with open d-, p-, and s-shells (Banerjee et al. 2020).

The energy level density for the elements with the same open shell becomes the maximum when the open shells are half-filled. This is because the half-filled shells have the maximum complexity. For example, for the elements with an open d-shell at the ionization state of IX (Ir–Rn, $Z = 77$–86), the maximum energy level densities appear around Tl–Po ($Z = 81$–83), where the open d-shell is nearly half-filled (Table B1). Similar trends are observed for the elements with the other open shells, e.g., the elements with a p-shell and s-shell across different ionizations.

In the case of the elements with an open f-shell at higher ionization, an open p-shell is also present. The number of electrons in the two open shells affects the energy level density distributions in different ways: (1) for a particular ionization,
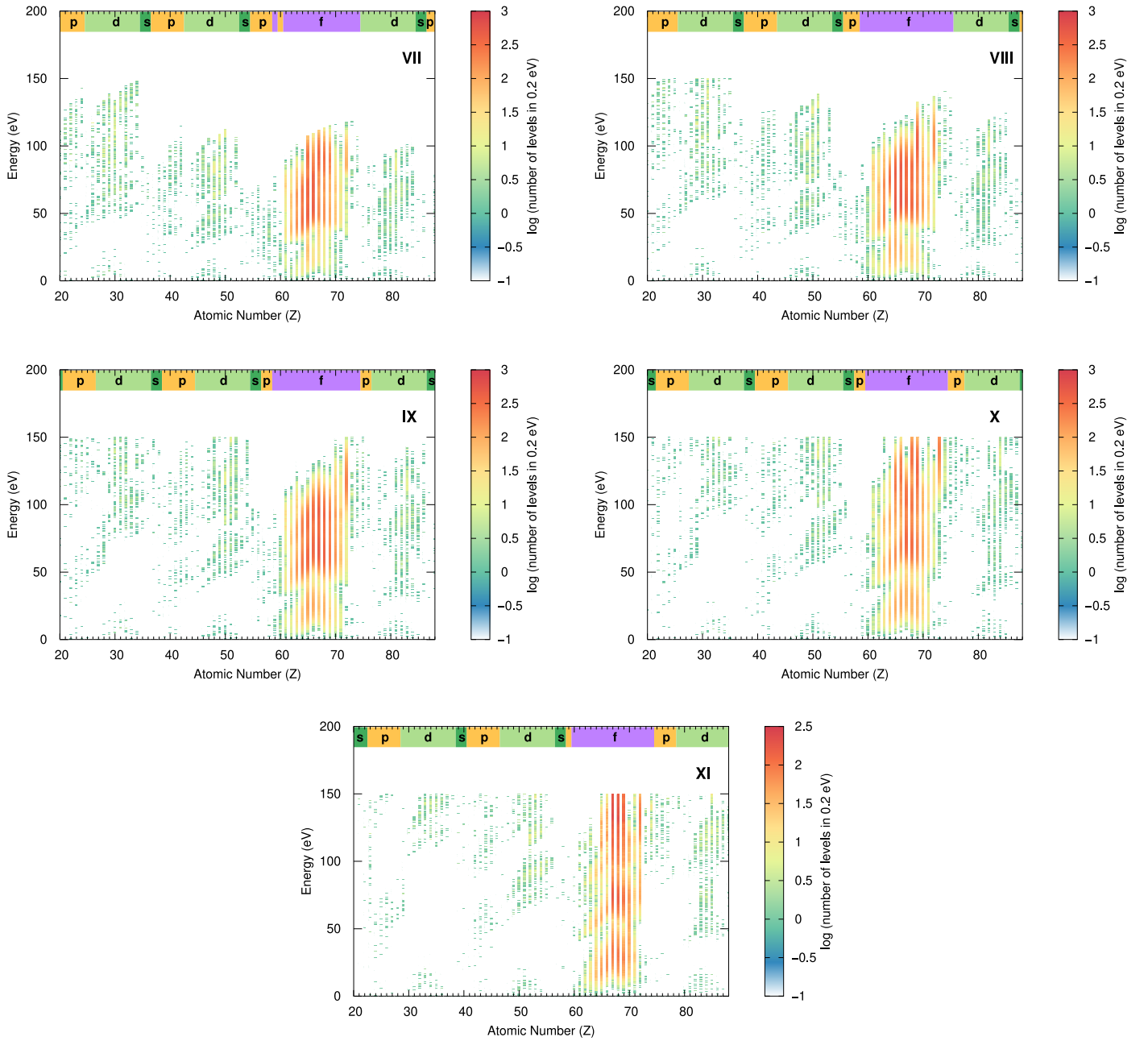
Figure 2. The same as Figure 1 but for the ionization states of VII–XI.

the number of electrons in the *f*-shell determines the elements that have the densest energy level density structure. For instance, the energy level density is the maximum for the elements Tb to Tm ($Z = 65$–69, see Figures 1 and 2), which have the nearly half-filled *f*-shell (Table B1) across different ionizations; (2) for a particular element, the number of electrons in the *p*-shell determines the ionizations at which the energy level density reaches its maximum. As an example, consider Eu, for which the energy level density distribution is the maximum around the ionization VIII–X (Figure 2), where the *p*-shell is nearly half-filled (Table B1). If both the shells are half-filled, as in the case for the elements Tb–Tm ($Z = 65$–69) at the ionization states of ∼VIII–X, then they show the highest energy level densities among all the different lanthanide ions (Figures 1 and 2).

Figure 3 shows the total number of transitions for different elements (N_{line} in Table B1) in various ionization states (V–XI). The labels provide the valence shells for the element with the highest number of transitions at particular ionizations (note that we do not specify the ions with *s*-shell explicitly; nevertheless, these can be found in Table B1). The lighter *r*-process elements ($Z \leqslant 56$, Banerjee et al. 2020) and the three lanthanides (Nd, Sm, Eu, Banerjee et al. 2022) are also shown for comparison.

The trend in the total number of transitions reflects the number density of the energy levels (Figures 1 and 2). For instance, at any particular ionization, the number of transitions is consecutively lower for the elements with open *f*- and *p*-shells, followed by the elements with open *d*-, *p*-, and *s*-shells (Figure 3). Moreover, the transitions for the elements with the same open shells become the maximum when the open shells
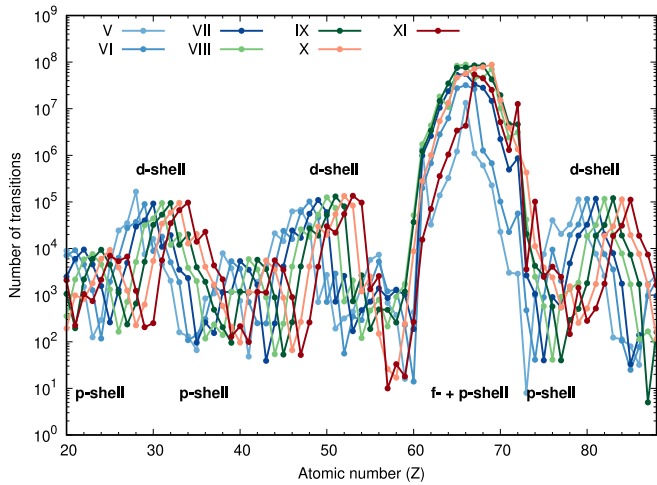
Figure 3. Number of transitions for the ionization V–XI for all the elements from Ca ($Z = 20$) to Ra ($Z = 88$).

are half-filled. This is due to the fact that the ions with half-filled shells show the largest number of energy levels and transitions.

For a few of the highly ionized elements (VII–XI) with an open f-shell and p-shell, the total number of transitions involving all the energy levels (N_{line}^{*} in Table B1) is higher than the transitions involving the energy levels only below the ionization threshold (N_{line} in Table B1, e.g., see Tb VIII in Table B1). This can be understood in the following way. First, most of these ions have high complexity due to the presence of open f-shell and p-shell; hence, the total number of energy levels is extremely high. Also, for these ions, the energy levels are pushed upward due to several effects, such as the higher degree of ionization and higher spin–orbit interaction (Cowan 1981; Tanaka et al. 2020). Combining these two effects, the transitions involving the higher-lying energy levels beyond the threshold energy increase significantly.

2.3. Bound–Bound Opacity

Using the newly constructed atomic data, we calculate the expansion opacity for all the elements La–Ra ($Z = 57–88$) ionized to the states of V–XI. We assume single-element ejecta with the density $\rho = 10^{-10}$ g cm^{-3}, which represents the ejecta condition at $t \sim 0.1$ day for an AT2017gfo-like neutron star merger ejecta with an ejecta mass of $M_{\mathrm{ej}} \sim 0.05\,M_{\odot}$ (Kasen et al. 2017; Kasliwal et al. 2017; Waxman et al. 2018; Banerjee et al. 2020), moving with an average velocity of $v_{\mathrm{avg}} \sim 0.1c$ (e.g., Tanaka et al. 2017). The single-element ejecta is not realistic as the ejecta always contain a mixture of elements. However, we discuss the single-element opacity to understand the effect of the newly calculated atomic data on the opacity.

At early time, the outermost layer opacity determines the shape of the light curves (Banerjee et al. 2020, 2022). The temperature of the outermost layer for the ejecta of the AT2017gfo-like neutron star merger ejecta moving with a velocity of $v \sim 0.2c$ (e.g., Tanaka et al. 2017) is $T \sim 70,000$ K (Banerjee et al. 2020). Since our main aim is to provide the light curve for the early kilonova, we chose this temperature to discuss the expansion opacity. Around the temperature of $T = 70,000$ K, the elements become IX ionized.

The expansion opacities for different elements at a temperature of $T = 70,000$ K are shown in Figure 4. The

expansion opacities show a strong wavelength dependence, with a higher value at the shorter wavelengths ($\lambda < 1000$ Å). This is because of the higher number of transitions at shorter wavelengths.

The expansion opacities for the elements with different shells vary widely. For example, the opacities for the elements with open f- and p-shells ($Z = 59–73$ at ionization IX, relevant at temperature $T \sim 70,000$ K) are extremely high, reaching $\kappa_{\mathrm{exp}} = 3 \times 10^3$ cm^2 g^{-1} at $\lambda \leqslant 1000$ Å, followed by the elements with open d-shells ($Z = 77–86$ at ionization IX), an open p-shell without an f-shell ($Z \sim 74–76$ at ionizations IX), and with an open s-shell ($Z \sim 87–88$ at ionization IX), with the opacity reaching $\kappa_{\mathrm{exp}} = 1.0$, 0.1, and 0.01 cm^2 g^{-1}, respectively, at the same wavelengths.

The wide range of the expansion opacities across the elements with different valence shells stems from the differences in the energy level density (and correspondingly, the number of transitions) in the presence of the different open shells (see Section 2.2). Note that this is different from the low-ionization case (e.g., Tanaka et al. 2020), where the density of those energy levels determines the opacity because only the low-lying energy levels are populated at lower ionization (i.e., at low temperatures). Hence, the number density of the low-lying energy levels determines the opacity. On the other hand, in the highly ionized state (i.e., at a higher temperature), even the higher energy levels can be populated. Hence, the total energy level density is more important in determining the opacity.

We discuss the limitation of the opacity calculation before proceeding further. For the expansion opacity in the neutron star mergers, the contribution of multiple lines is taken into account under the assumption that the interactions between the photons and lines are independent of each other. This assumption requires the photons to travel freely between the two different interactions with different lines. Such an assumption works fine as long as the resonance zones or the line profiles do not overlap each other. However, if the line profiles start to overlap with each other, assuming the expansion opacity underestimates the opacity. This is because, in such cases, taking the expansion opacity overestimates the photon mean free path by assuming independent interactions.

To indicate when the line profiles start overlapping, a critical opacity is defined as $\kappa_{\mathrm{crit}} \sim 3\,\rho_{-10}^{-1}\,v_{\mathrm{th},4}^{-1}\,t_{0.1}^{-1}$ cm^2 g^{-1} (Kasen et al. 2013; Banerjee et al. 2022), where $\rho_{-10} = \rho/10^{-10}$ g cm^{-3}, $v_{\mathrm{th},4}$ is the thermal velocity $v_{\mathrm{th}}/4$ km s^{-1}, the typical values at $t_{0.1} = t/0.1$ day. If the expansion opacity is higher than this critical value, that implies that the line profiles start overlapping. The expansion opacities for the elements with an open f-shell or the lanthanides are higher than the critical value at the far-UV ($\lambda \leqslant 1000$ Å). Hence, the opacities in the far-UV wavelengths for the lanthanides are mostly underestimated.

Keeping the limitation of the opacity calculation in mind, we calculate the Planck mean opacities to study the temperature dependence of the expansion opacity. For that purpose, we convolve the expansion opacities with the blackbody function. Note that the Planck mean opacity is underestimated for the lanthanides at higher temperatures since the blackbody function peaks at the far-UV at higher temperatures, where the expansion opacity exceeds the critical opacity.

The peaks of the opacity for lanthanides appear at $T \sim 70,000–90,000$ K (Figure 5). This is because lanthanides become $\geqslant$VII ionized around this temperature, where the ions
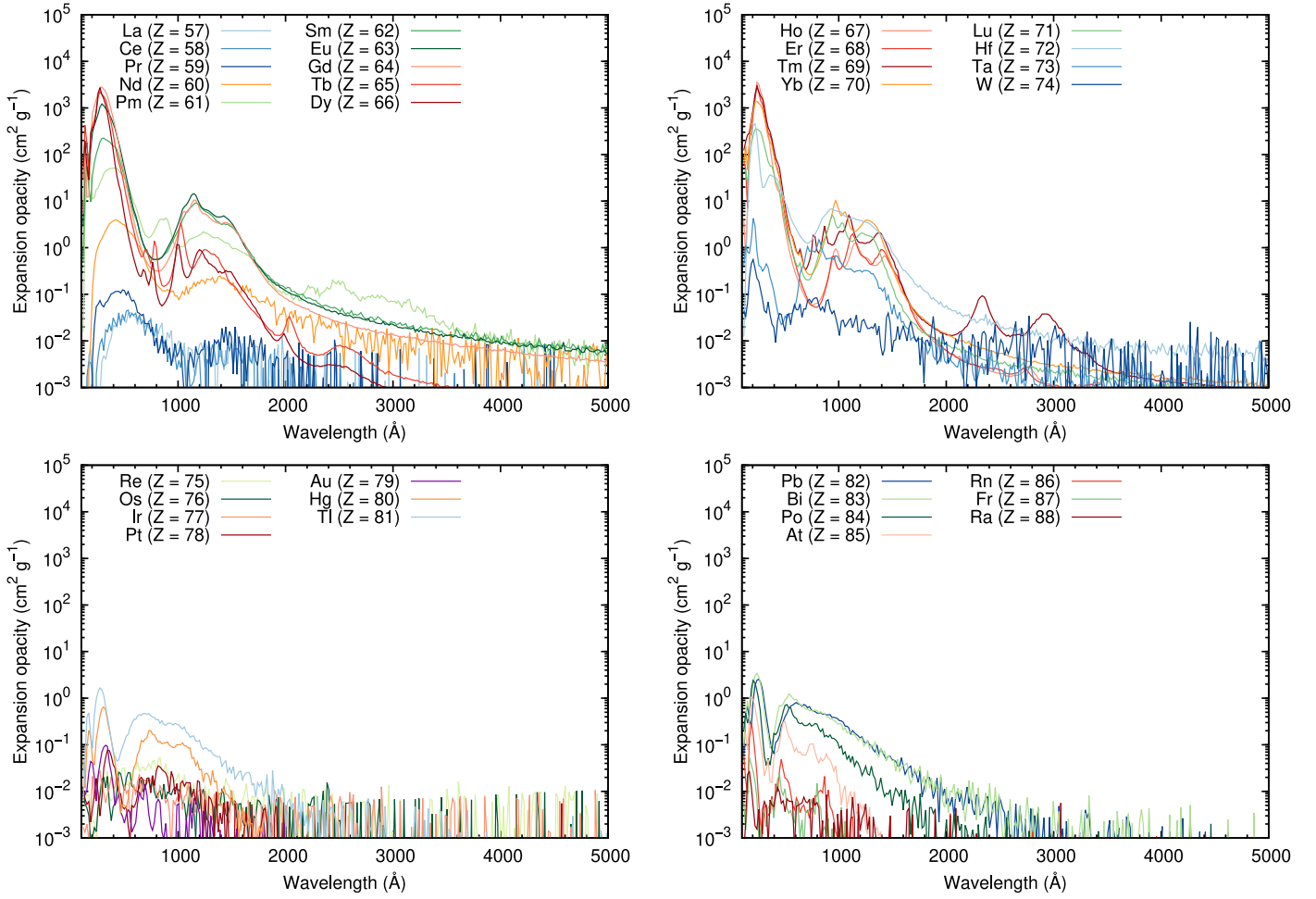
Figure 4. The expansion opacity as a function of wavelength at $T = 70,000$ K, $\rho = 10^{-10}$ g cm^{-3}, and at $t = 0.1$ day for the different elements.

have two open shells (*f*- and *p*-shells, Table B1). Note that for different lanthanides, the ionization of ≥VII appears at nearly the same temperature since the potential energy does not vary much between lanthanides. Moreover, among the lanthanides with ionization ≥VII, the maximum value of the opacity appears for the elements Tb to Tm ($Z = 65$–69), which have two open shells nearly half-filled at such ionizations.

For the elements with other valence shells (*d*-shell, *p*-shell without *f*-shell, and *s*-shell), the maxima in the opacity appear whenever the valence shells become half-filled (Figure 5). For example, at $T \sim 10^5$ K, Re ($Z = 75$) shows the maxima in opacity (see Figure 5). This is because at this temperature, Re is ionized to ~XI, where the valence *p*-shell is nearly half-filled. The same trend is also observed for the *d*-shell, *p*-shell without *f*-shell, and *s*-shell elements for the lighter *r*-process elements (Banerjee et al. 2020).

The overall variation in the Planck mean opacities for the elements is illustrated in the right panel of Figure 6, which shows the Planck mean opacities at the temperatures of $T = 25,000$, $50,000$, $70,000$, and $90,000$ K. Note that these are the temperatures where the peak of the ionization states of V, VII, IX, and XI appear. It is clear that the valence shells for different elements change with ionizations (left panel of Figure 6), and affects the overall opacity. Note that the peak opacity in the elements with the two open shells (open *f*- and *p*-shells) is underestimated due to taking the assumption of the expansion opacity.

We discuss the opacity trends for a single-element ejecta with a fixed density. However, such conditions are not realistic for the neutron star merger ejecta since the neutron star merger ejecta consists of a mixture of elements. Also, as the ejecta expands with time, the density and temperature change, causing the change in the opacity. We discuss the opacity of the mixture of elements for the realistic ejecta conditions in the context of the radiative transfer simulations in the next sections.

3. Radiative Transfer Simulations

3.1. Models

In the binary neutron star merger, the elemental distribution dominantly depends on the electron fraction (Y_e), i.e., the electron-to-baryon ratio in the ejecta. In neutron star mergers, masses are ejected in several different channels (Shibata & Hotokezaka 2019), producing multiple ejecta components. Different ejecta components have different electron fractions. For the dynamical ejecta, the mass ejected toward the polar direction, due to the shock between the interface of the neutron stars, has a relatively higher electron fraction ($Y_e > 0.25$, e.g., Bauswein et al. 2013; Just et al. 2015; Sekiguchi et al. 2015; Just et al. 2022), whereas the mass ejected due to the tidal disruption of the neutron stars have relatively lower electron fraction ($Y_e < 0.25$, e.g., Bauswein et al. 2013; Just et al. 2015, 2022; Sekiguchi et al. 2015). Additionally, masses are ejected (more isotropically) from the disk formed around the
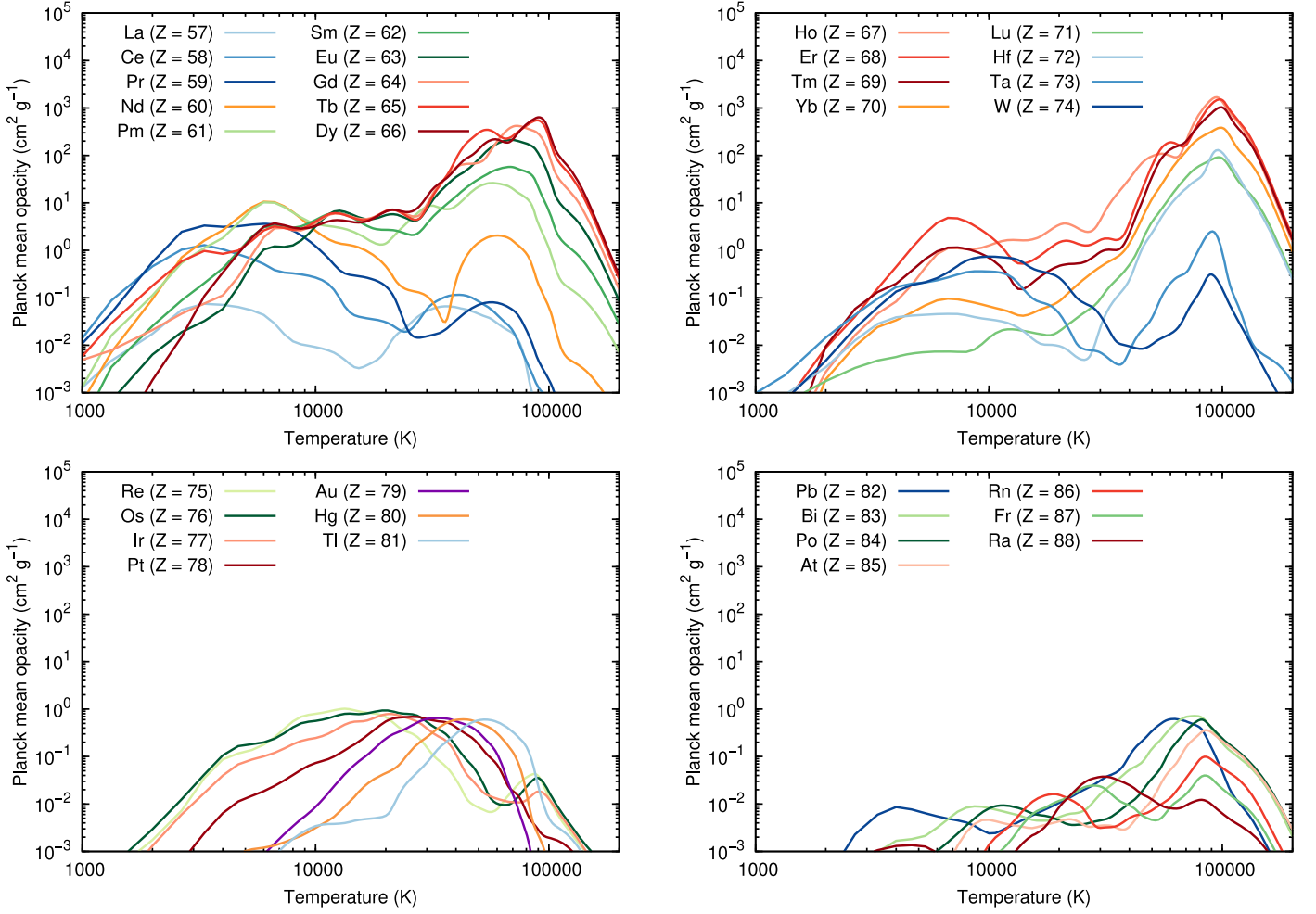
Figure 5. The Planck mean opacity as a function of temperature at $\rho = 10^{-10}$ g cm^{-3} and $t = 0.1$ day for different elements.
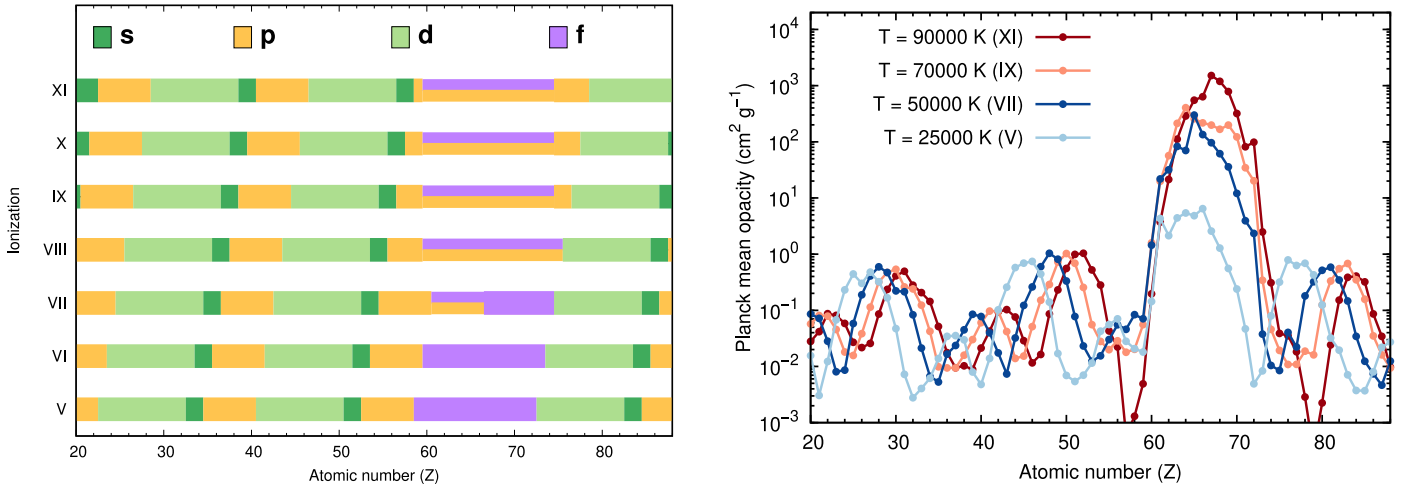
Figure 6. Left: the change in the valence shell with ionization for different elements. Note that the s-, p-, d-, and f-shells are represented by the colors dark green, yellow, light green, and purple, respectively. Right: the mean opacity for different elements. Different colors represent different temperatures.

central remnant in a longer timescale. This disk wind ejecta has a relatively higher electron fraction, due to the higher neutrino irradiation (e.g., Fernandez & Metzger 2014; Metzger & Fernández 2014; Perego et al. 2014; Lippuner et al. 2017; Fujibayashi et al. 2018, 2020a, 2020b; Miller et al. 2019). Differences in the electron fraction introduce variance in the elemental abundance pattern in different ejecta components,

which introduces a viewing angle dependence in the kilonova light curves.

To understand the early kilonova for different compositions, we perform radiative transfer simulations for a 1D spherical ejecta model (Metzger et al. 2010) with a power-law density structure of $\rho \propto r^n$, where $n = -3$, moving within the velocity range of $v = 0.05c$–$0.2c$. The electron fraction is taken to be
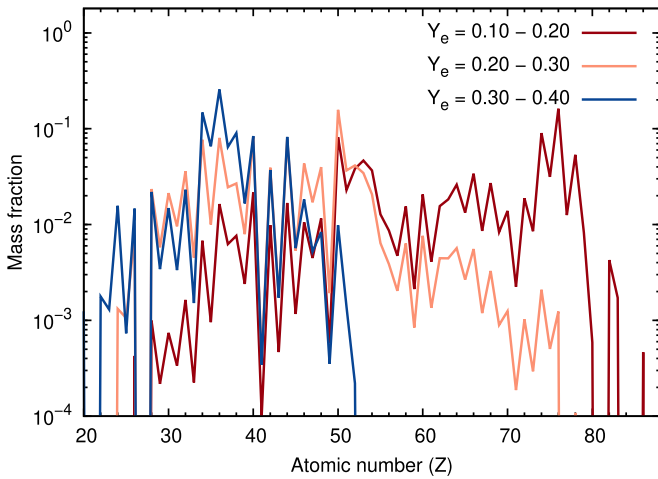
Figure 7. The abundance pattern for different electron fractions. The data are taken from Wanajo et al. (2014).

homogeneous with the values (1) $Y_e = 0.10$–0.20; (2) $Y_e = 0.20$–0.30; and (3) $Y_e = 0.30$–0.40. The first two of our models correspond to the viewing angle more toward the equatorial plane, whereas the last model corresponds to the abundances expected for the viewing angle more toward the polar direction. Note that the abundances are derived from Wanajo et al. (2014), taking a flat mass distribution for each value in the Y_e range (see Figure 7). The percentage of the lanthanide abundance in the ejecta for the three different models are ∼21%, ∼4.8%, and ∼0%, respectively. The total ejecta masses for the models are fixed at $M_{ej} = 0.01\,M_\odot$. Note that model 3 is the same as the fiducial model used in Banerjee et al. (2020), but with lower ejecta mass ($M_{ej} = 0.01\,M_\odot$ instead of $M_{ej} = 0.05\,M_\odot$).

Our choice of models in 1D is relatively simple. In reality, the observer from the polar direction would observe the emission from the lanthanide-free disk wind ejecta surrounded by the faster moving lanthanide-free polar dynamical ejecta. Similarly, the observer from the equatorial direction would observe the emission from the lanthanide-free disk wind ejecta surrounded by the lanthanide-rich, faster moving tidal dynamical ejecta.

To study the effects of the density and the abundance structure in the ejecta, we also include additional models with a continuous thin outer layer with a fixed mass of $M_{out} = 0.001\,M_\odot$, moving at a velocity of $v > 0.2c$. The layer has a steeper density structure $\rho \propto r^{n'}$. We take $n' = -10$ since such profiles show a good fit with the last kilonova AT2017gfo associated with GW170817 (Kasen et al. 2017). In this case, the maximum outer velocity is $v \sim 0.33\,c$. The electron fraction of the inner layer ejecta ($v \leqslant 0.2c$) is fixed to be $Y_{e,in} = 0.30$–0.40, but the same for the outer layer ejecta ($0.2c < v \leqslant 0.33c$) are varied and are assumed as different models: (4) $Y_{e,\,out} = 0.10$–0.20; (5) $Y_{e,\,out} = 0.20$–0.30; and (6) $Y_{e,\,out} = 0.30$–0.40. These models are the more realistic situation for the viewing angles toward the equatorial (models 4 and 5) and the polar direction (model 6). We summarize all the models in Table 1.

To calculate the light curves, we use a time- and wavelength-dependent Monte Carlo radiative transfer code (Tanaka & Hotokezaka 2013; Kawaguchi et al. 2018). The code calculates the multicolor light curves and spectra for a given density structure and electron fraction (Y_e) distribution, assuming a

homologously expanding motion of the ejecta. The radioactive heating rate of the r-process nuclei is calculated according to Y_e, by using the results from Wanajo et al. (2014). The code adopts a time-dependent thermalization factor from Barnes et al. (2016). Our simulation considers the wavelength range of $\lambda \sim 100$–35000 Å.

Here, we want to mention that the radiative transfer becomes infeasible if we use the complete line list, including the highly ionized lanthanides. This is because the number of transitions is extremely high. Hence, to make the line list for the lanthanide ions, we include a reduced number of transitions for the ionization $> V$. To reduce the line lists, we follow a method introduced by Banerjee et al. (2022). We randomly select the transitions from the original line list by keeping the statistical properties the same. Following Banerjee et al. (2022), we use 0.1% of the total line list to perform radiative transfer simulations since such a reduced line list is confirmed to preserve the statistical properties. More details of the method can be found in Banerjee et al. (2022). Note that for the elements with the ionization $\leqslant$ IV, we use the non-reduced complete atomic data from Tanaka et al. (2020).

Note that to reduce the line lists, some previous works (e.g., Fontes et al. 2020) only considered lines with an oscillator strength above the prescribed threshold value. In this paper, we use the alternative method to reduce the line list. This is because, using our method, we can achieve a more significant reduction of the line list without any trade-off in accuracy. Hence, the computational efficiency increases using this method.

Our models assume ejecta masses smaller than that proposed for the kilonova AT2017gfo ($M_{ej} = 0.05\,M_\odot$, e.g., Kasen et al. 2017; Kasliwal et al. 2017; Waxman et al. 2018; Banerjee et al. 2020). This is because our work aims to provide conservative estimates for the brightness of the kilonova emission. Due to this choice, the physical properties, and correspondingly, the opacity of the ejecta might be different than the single-element opacity discussed in Section 2.3. Therefore, we first discuss the evolution of the opacity for these models.

3.2. Opacity Evolution

As the ejecta expands with time, the density and the temperature evolve. The change in the temperature causes the change in the ionization, and correspondingly, changes the opacity. At early time, the physical conditions of the ejecta at the outermost layer mainly affect the light curve since most of the emission comes from the outermost layer in the ejecta at early time.

Figure 8 shows the physical conditions (density, temperature) of the ejecta at the outermost layers in the ejecta for the different models. The outermost layer for the models with the simple density (e.g., model 3) and the models with the continuous thin outer layer (e.g., model 6) are different. Hence, we show the physical conditions at $v = 0.19c$ for the model with the simple density structure (e.g., model 3, orange curves in Figure 8) and at $v = 0.33c$ for the models with the additional thin layers (e.g., model 5, blue curves in Figure 8). The labels in the right panel of Figure 8 show the peak ionization appearing at different temperatures.

The density and the temperature in the outer layer of the ejecta for the simple ejecta model (e.g., model 3) varies from 10^{-10}–10^{-14} g cm^{-3} and $T \sim 90{,}000$–$10{,}000$ K, respectively, during the time from $t \sim 0.05$ to ∼1 day. The corresponding
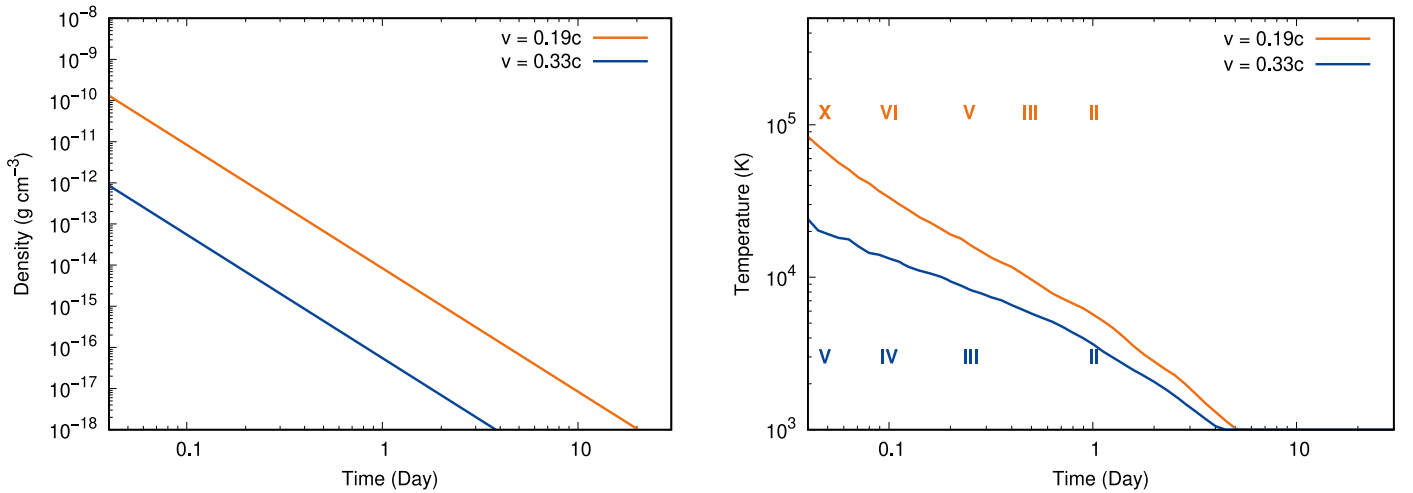
Figure 8. The density (left) and the temperature (right) evolution at the fixed ejecta point, $v = 0.19c$ and $0.33c$ for model 3 (orange) and model 6 (blue), respectively. In the presence of the lanthanides in the ejecta, the light curves are fainter. Also, the light curves are affected by the thin outer layer in the ejecta.

Table 1
Models and the Corresponding Gray Opacities

Models	Electron Fraction		Suggested Gray Opacities $(cm^2\,g^{-1})$
	$Y_{e,\ in}$ $(v = 0.05c - 0.2c,\ M_{ej,in} = 0.01\ M_\odot)$	$Y_{e,\ out}$ $(v = 0.2c - 0.33c,\ M_{ej,out} = 0.001\ M_\odot)$	
Model 1	0.10–0.20	⋯	2.0–10.0
Model 2	0.20–0.30	⋯	1.0–5.0
Model 3	0.30–0.40	⋯	0.8
Model 4	0.30–0.40	0.10–0.20	5.0–10.0
Model 5	0.30–0.40	0.20–0.30	3.0–5.0
Model 6	0.30–0.40	0.30–0.40	0.8

ionization varies from X to II. The outermost layer of the ejecta for the model with a thin layer (e.g., model 6) has a lower density, and correspondingly, lower temperature and ionization. The other models with the same density structure show almost the same trends for the temperature (and hence the ionization) evolution in the outermost layers, although there might be slight variation due to the differences in the compositions in different models.

The expansion opacity evolves with the changes in the physical conditions (temperature and density) in the ejecta. The top panel of Figure 9 shows the evolution of the expansion opacity at the outer layers ($v \sim 0.19c$) for models 2 and 3, i.e., the simple models with and without lanthanides. Note that we show the opacity only for one lanthanide-rich model (model 2, with lanthanide, the fraction is 4.8 %) since the evolution is similar in the other lanthanide-rich model (model 1, with lanthanide, the fraction is 21 %), except for the fact that the opacity is higher due to the higher lanthanide abundances.

The opacity for the mixture of the elements in the ejecta shows a strong wavelength dependence similar to that of the opacity for the individual elements. The opacity for the ejecta containing lanthanides shows an extremely high value ($\kappa_{exp} \sim 3 \times 10^3\ cm^2\,g^{-1}$) at around $\lambda \leqslant 1000\,\text{Å}$ at $t \sim$ 0.05–0.1 day, which is much higher than the expansion opacity for the lanthanide-free ejecta (the peak value of $\kappa_{exp} \sim$ 1–10 $cm^2\,g^{-1}$ at $\lambda \leqslant 1000\,\text{Å}$) at the same time. This is because at around $t \leqslant 0.1$ day, the outer ejecta reaches the temperature

range ($T \geqslant 50,000$ K, Figure 8) suitable for the lanthanides to be ionized at $\geqslant$VII, which shows the maximum energy level density (see Section 2.2).

As time progresses, the wavelength-dependent opacity in the outer layer of the ejecta changes due to the changes in the ionization. For example, the peak in the far-UV wavelengths ($\lambda \leqslant 1000\,\text{Å}$) for the lanthanide-rich ejecta disappears with time as the temperature, and hence, the ionization decreases. In addition, the opacity values shift toward higher values because of the changes in the density toward the lower value (see Equation (1)).

The bottom panels of Figure 9 show the opacity in the outermost layer ($v \sim 0.33c$) for models 5 and 6, where the lanthanide-rich and lanthanide-free continuous thin outer layer is present. Interestingly, for the lanthanide-rich ejecta (model 5), the signature high opacity peak at far-UV wavelengths ($\lambda \leqslant 1000\,\text{Å}$) is not observed. This is because the outermost layer is relatively less dense, and the temperature is lower than that at $v = 0.19c$ in the models with the simple density structure, i.e., models 1–3. Hence, the temperature range, where the lanthanides are highly ionized ($\geqslant$VII) is passed before $t < 0.03$ day, the earliest epoch in our simulation. Similarly, the opacity in the outermost layer for the lanthanide-free models can be understood.

In the recent study calculating the kilonova signal for the equal-mass binary merger by Combi & Siegel (2023), they found that the high opacity peaks for lanthanides do not appear
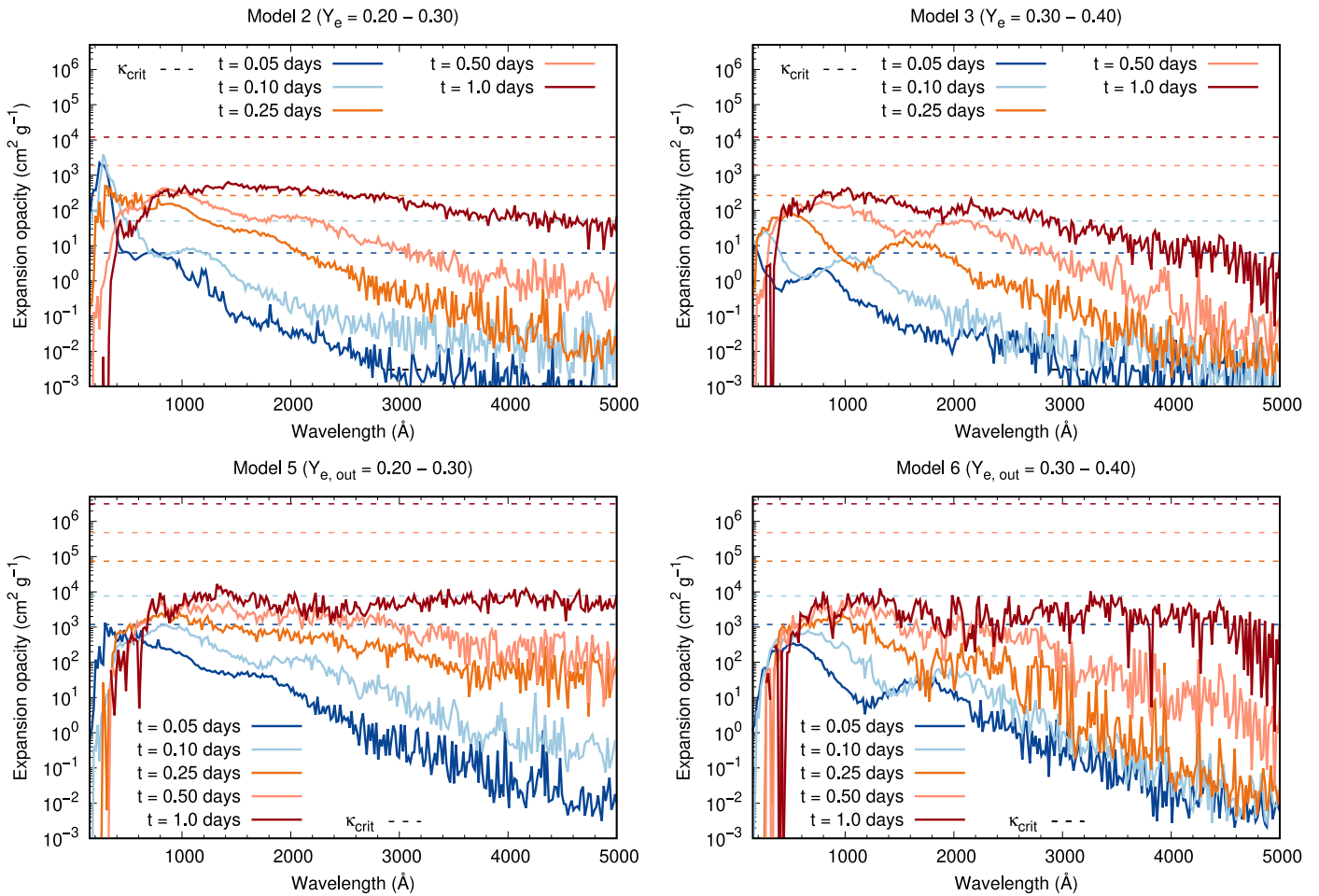
Figure 9. The expansion opacity evolution at the fixed point of ejecta for different models: $v = 0.19c$ in models 2 and 3 with simple density (top panel); $v = 0.33c$ in models 5 and 6 with a continuous thin outer layer density structure (bottom panel). The ejecta for models 2 and 5 are lanthanide-rich, and those for models 3 and 6 are lanthanide-free. The high peak in the opacity is seen only for the lanthanide-rich model with the simple density structure (model 2). The critical opacities at the fixed ejecta point at different times are also shown (dashed lines). The expansion opacity approximation is good when the expansion opacities are lower than the critical opacities. This condition is satisfied for most of the models at different timescales. The only exception is the opacity for model 2 at $\lambda \leqslant 1000$ Å at $t < 0.25$ day, when the expansion opacity is underestimated.

at early time ($t \sim 1$ hr) for the ejecta at the high-velocity tail. Interestingly, our results for the model with a lanthanide-rich thin outer layer (model 5), show behavior similar to their result despite a different ejecta distribution. This is mainly due to the fact that the total mass of the ejecta considered in both simulations is comparable (within a factor of a few). However, for different merger conditions, e.g., for a merger of binaries with higher mass ratios, the mass of the dynamical ejecta might be higher (Fujibayashi et al. 2023), resulting in a higher temperature in the outer layer of the ejecta until a time of approximately a few hours. In such a case, the high opacity peaks of lanthanides may significantly affect the opacity and the light curves.

Finally, we discuss the limitations of our opacity calculations. We use expansion opacity approximation for our opacity calculations. However, if the expansion opacity is beyond the critical opacity at a particular density and temperature, then the opacity is underestimated (Section 2). We show critical opacities at different times as dashed lines in Figure 9 to assess whether the expansion opacity provides a good approximation at different times.

Our results show that the expansion opacity provides a good approximation over the entire wavelength range considered across different epochs for all the realistic models with thin, continuous outer layers (models 4–6, Figure 9). In addition, the expansion opacity provides a good approximation for the model with a simple density structure and with no lanthanide abundances (model 3). The only exception occurs for the models where the ejecta have the simple density structure and the lanthanide-rich abundances (e.g., model 2) at the earliest epoch ($t < 0.25$ day) at far-UV wavelengths ($\lambda \leqslant 1000$ Å), when the expansion opacity exceeds the critical opacity. Hence, the opacity is underestimated for models 1 and 2 at $t < 0.25$ day at the far-UV ($\lambda \leqslant 1000$ Å). However, even in such cases, we can calculate the effective upper limits of the light curves at the far-UV, whereas the light curves at longer wavelengths are expected to be unaffected.

Here, we also note that in our calculation, we neglect the actinides ($Z = 89$–103), while calculating the abundance pattern for the ejecta with a lower electron fraction. Hence, the overall opacity might be underestimated. For example, the calculation from Wanajo et al. (2014) shows that if the electron fraction in the ejecta is $Y_e = 0.10$–0.20, the ejecta can contain up to 2% of actinides ($Z = 89$–103). Hence, our results of atomic opacity might be underestimated for the models

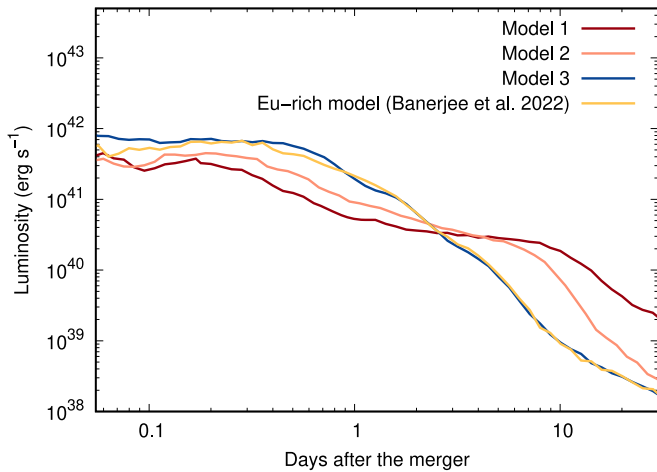**Figure 10.** Bolometric luminosity for different models with simple density and different abundances (different colored curves). The ejecta with simple density and single lanthanide elemental abundance (10% Eu, Banerjee et al. 2022) is shown for comparison. If the lanthanides are present in the ejecta, they show a unique rising signature at early time. Also, for the lanthanide-rich ejecta, the overall light curve is fainter than the lanthanide-free case.

Figure 11. Bolometric luminosity for different models with simple density (dashed lines) and the models with the additional thin layer (solid lines). Different colored curves represent the models with different compositions.

including the ejecta with $Y_e = 0.10$–0.20, such as models 1 and 4.

3.3. Bolometric Light Curves

Figure 10 shows the bolometric luminosities for different models with the simple density structure (models 1–3). Additionally, the luminosity for the ejecta with the same density structure but the composition consisting of the mixture of a single lanthanide Eu ($Z = 63$, with an abundance of ∼10%) and the light r-process elements (corresponding to the electron fraction $Y_e = 0.30$–0.40) is shown for comparison. Note that this is the same model adopted in Banerjee et al. (2022), except for the lower ejecta mass considered in this work.

The bolometric luminosities for lanthanide-rich models (models 1 and 2, maroon and orange curves, Figure 10) are fainter in comparison with the luminosities of the lanthanide-free model (blue curve in model 3, Figure 10). The bolometric luminosities for the lanthanide-rich ejecta (models 1 and 2) reach ∼$L_{\rm bol} \sim 3$–4×10^{41} erg s^{-1} at $t \sim 0.2$ day, where the higher luminosity is for the lower fraction of lanthanides (model 2) in the ejecta. On the other hand, the bolometric luminosities for the ejecta with no lanthanides (model 3) reach $L_{\rm bol} \sim 8 \times 10^{41}$ erg s^{-1} at $t \sim 0.2$ day. The faintness of the light curves in lanthanide-rich models is observed at the later epochs as well. This is because the presence of the lanthanides makes the opacity in the ejecta higher at all epochs (see Figure 9), consequently making the light curves fainter.

The bolometric luminosities for the lanthanide-free ejecta (model 3) are relatively flat at times $t < 1$ day, whereas that for lanthanide-rich models (models 1 and 2) show distinct signatures at the same epochs (Figure 10). For instance, the light curves for the lanthanide-rich models (models 1 and 2) are fainter than the lanthanide-free one by a factor of ∼8 around $t \sim 0.1$ day; after which the light curves rise until $t \sim 0.2$ day and decrease afterward. Therefore, the trend in the bolometric luminosities before $t \sim 1$ day can act as a distinct signature to infer the presence of the lanthanides in the ejecta.

The shape of the light curves for the lanthanide-rich ejecta at early time can be understood by the opacity evolution in the
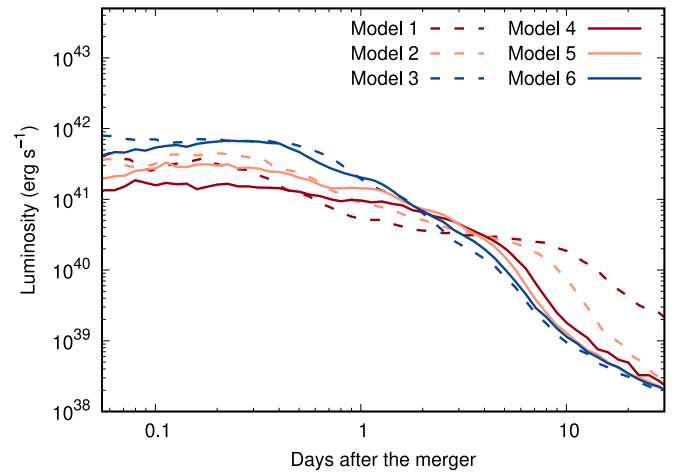
outer layer of the ejecta. At $t \leqslant 0.1$ day, the temperature of the outermost layer provides a suitable condition ($T \leqslant 70{,}000$ K) so that the opacity of the lanthanide-rich ejecta reaches the maximum opacity (see Section 3.2). Such a rise in the opacity in the outermost layer causes the luminosity to drop at $t < 0.1$ day. At around $t \sim 0.2$ day, the opacity in the outer layer of the ejecta decreases with the change in the temperature and ionization, causing the rise in the luminosity. This work, for the first time, provides the light curves for the realistic abundance pattern of the lanthanide-rich ejecta.

Note that previously, Banerjee et al. (2022) showed the effect of the lanthanides in the ejecta produces a distinct signature on the light curve. However, their model consists of a single lanthanide (e.g., Eu) instead of a mixture of lanthanides. We show that such a single lanthanide-rich model (Eu-rich model, similar to that in Banerjee et al. 2022, but with lower mass) can reproduce the overall trend of the early luminosity at $t < 0.2$ day as the model with the mixture of lanthanides (Figure 10). However, the absence of the second half of the lanthanides overestimates the luminosity beyond $t > 0.2$ day.

The presence of a continuous, thin outer layer in the ejecta (models 4–6) makes the early luminosity fainter than that of the cases with the simple density structure (e.g., models 1–3, Figure 11). For example, the light curves for the models with lanthanide-free inner and outer ejecta (model 6) are fainter than those of the models with a simple density structure containing no outer layer ejecta (model 3, Figure 11). This is in agreement with the previous works by Kasen et al. (2017) and Banerjee et al. (2020). In the case where the outer layer contains lanthanides (e.g., model 5), the light curves are even fainter (Figure 11). Note that the presence of the lanthanides in the fast-moving thin outer layer in the ejecta produces light curves fainter than in the lanthanide-rich model with the simple density structure (e.g., model 2). Hence, there are possibilities for deducing the density structure as well as compositions from the shape of the light curves at early times.

The lower luminosity for the models with thin continuous outer layers (e.g., model 5) is mainly due to the lower density and correspondingly lower radioactive power deposited in the outer layer. The photons only escape from the outer layer at early time, and hence, the lower deposited power at the outer layer makes the light curves fainter. Note that the lower density
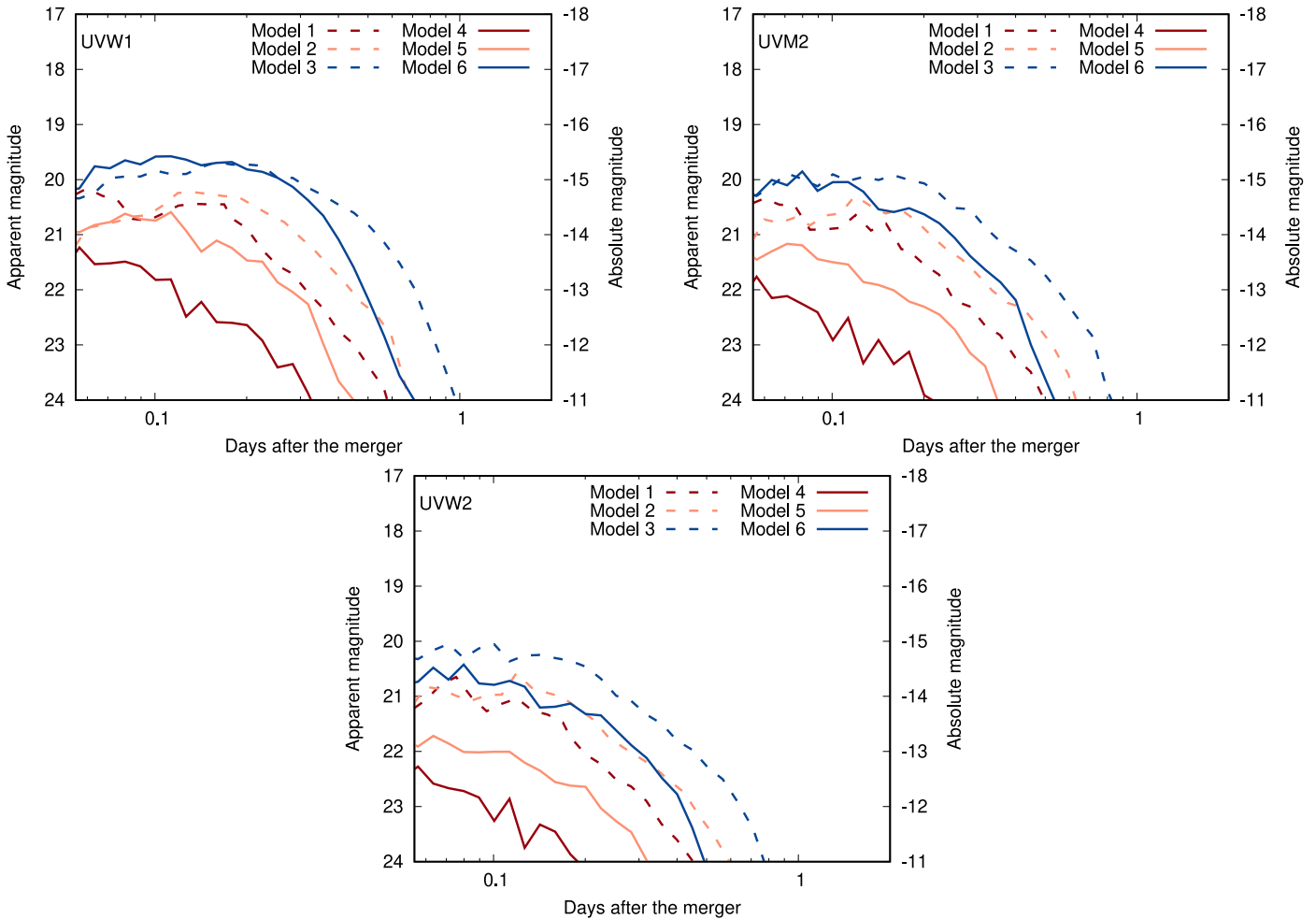
Figure 12. Comparison of UV magnitudes between different models for a source at a distance of 100 Mpc. The magnitudes are shown for three Swift filters, UVW2, UVM2, and UVW1, with the mean wavelengths of 2140, 2273, and 2688 Å, respectively (Roming et al. 2005). The light curves are fainter at $t \sim 0.1$ day if the lanthanides are present in the ejecta or if the thin outer layer is present.

in the outer layer is also the main reason for the lower luminosity, even for the models with the lanthanide-rich thin outer layer (e.g., model 5), and not the high opacity of the ejecta in the presence of lanthanides. In fact, in this case, the opacity in the outer layer is not extremely high even at the earliest epochs due to the lower density and lower temperature in the outer layer in such models (Figures 8 and 9).

Here, note that the temperature of the ejecta is mass dependent. If the ejecta mass (and correspondingly the outer layer mass) is high, the ejecta temperature is higher than that of the ejecta with lower mass. With the change in the mass and the temperature in the outer layer, the shape of the overall luminosity is expected to be affected.

3.4. Multicolor Light Curves

Figures 12 and 13 show the UV magnitudes in the three different Swift UVOT filters (UVW2, UVM2, and UVW1 with the mean wavelengths of 2140, 2273, and 2688 Å, respectively, Roming et al. 2005) and the four optical filters (g, r, i, z bands) for a source at 100 Mpc. The models with the simple density structure and that with the thin, continuous outer layer are shown by the dashed and solid lines, respectively.

For the models with the simple density (models 1–3), our results show that the UV brightness varies from $\sim$22–19.5 mag

at $t \sim 0.1$ day, fainter in the lanthanide-rich models (models 1 and 2). For the g, r, i, z filters, the early luminosity varies from $\sim$21–20 mag at around $t \sim 0.1$ day. The models with thin outer layers (models 4–6) are at the fainter magnitudes, similar to the behavior of the bolometric light curves.

The UV light curves are the promising observable signal at early time. If the kilonova is discovered early enough so that the prompt observation can be started, then the signals can be detected with the existing satellite Swift (with a limiting magnitude of $\sim$22 mag for an exposure time of 1000 s, Roming et al. 2005). The UV horizon will be broadened as many wide-field satellites such as ULTRASAT (limiting magnitude of 22.4 mag for 900 s of integration time, Sagiv et al. 2014), Dorado (limiting magnitude of 20.5 mag for 600 s of integration time, Dorsman et al. 2023), and UVEX (limiting magnitude of 25 mag for 900 s of integration time, Kulkarni et al. 2021) are upcoming in the next decade. Hence, in the near future, UV counterpart detection probability will increase manifold.

For the optical g, r, i, z filters, the brightness of the kilonovae for the lanthanide-rich ejecta is close to the detection limit of the existing observing facilities such as the Zwicky Transient Facility (ZTF; the limiting magnitudes for ZTF in g, r, i bands are 21.1, 20.9, and 20.2 mag, respectively, for the 30 s exposure time, Dekany et al. 2020). The detection of early
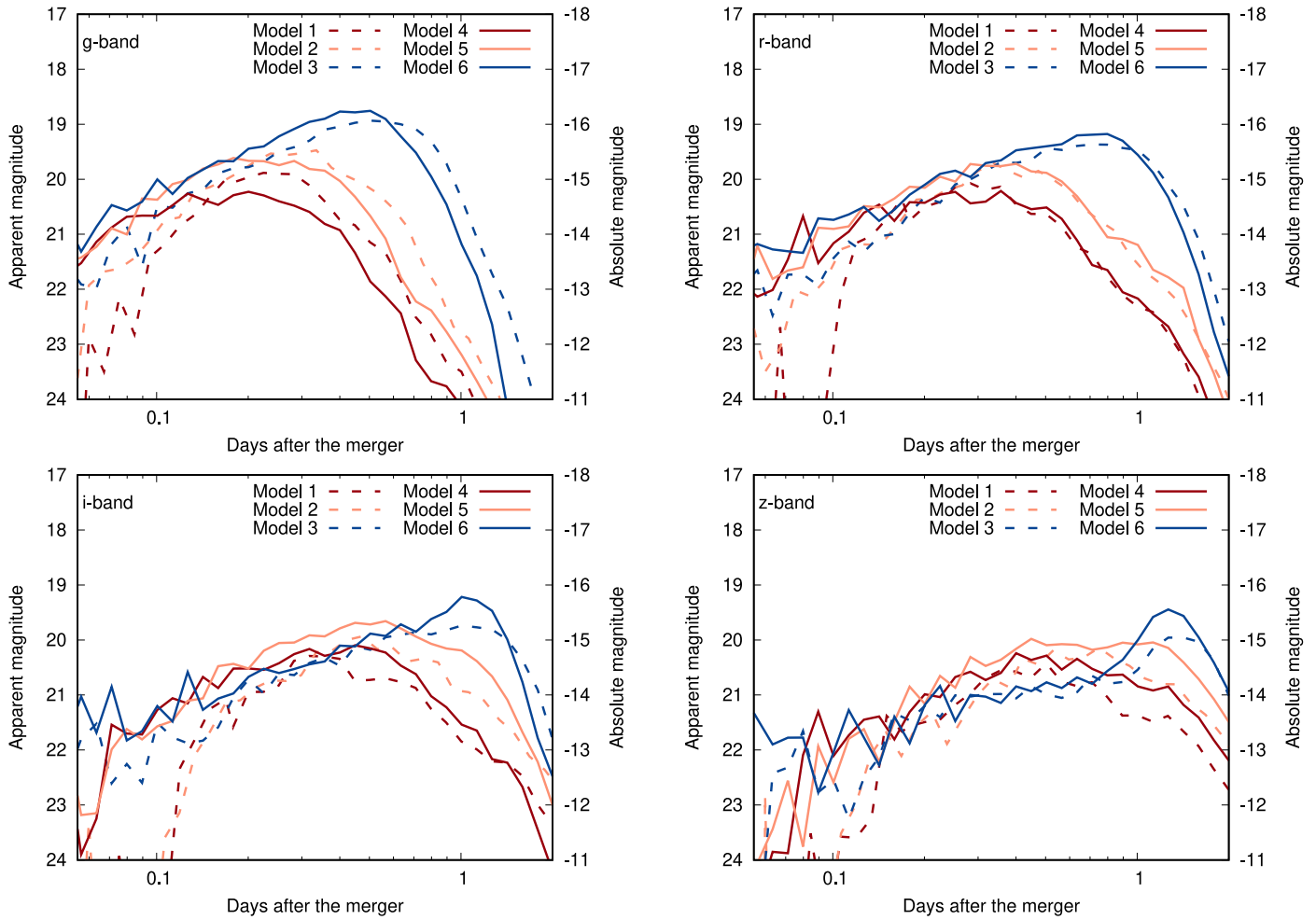
Figure 13. Comparison of magnitudes in four optical filters in the g, r, i, z bands for different models for a source at a distance of 100 Mpc.

kilonova in optical bands seems more feasible for the observing facilities with deeper observing limits, such as the Dark Energy Camera (DECam; the limiting magnitudes in the i, z bands are 22.5 and 21.8, respectively, for the 90 s exposure time, Chase et al. 2022) and the Subaru-Hyper Suprime-Cam (HSC), which can reach a depth of $\sim$24 mag for a 2×30 s exposure time (e.g., Ohgami et al. 2021, 2023). More promisingly, such signals in the optical bands can easily be detected by upcoming wide-field surveys, such as the Vera Rubin Observatory (Chase et al. 2022).

Here, we note that our opacity in the far-UV wavelengths does not provide the correct estimate; hence, our light curves are rather uncertain in the far-UV ($\lambda \leqslant 1000\,\text{Å}$) for the lanthanide-rich models with a simple ejecta structure. However, our light curves in the longer wavelengths are likely to be unaffected by this choice. Since the detection ranges of the existing instruments discussed here are all beyond 2000 Å (e.g., Swift, Roming et al. 2005), our models provide useful predictions for early kilonova.

4. Gray Opacities to Reproduce Early Kilonova

Several of the previous studies adopt gray, constant opacities to reproduce the early light curves of the kilonova AT2017gfo associated with GW170817. This is because of the absence of detailed opacities at early times. Since we perform the multifrequency transfer to calculate the early light curves for

kilonova using the detailed, wavelength-dependent opacity for almost all the feasible abundances, we now assess how good the gray approximations are at reproducing the early light curves. For this purpose, we perform radiative transfer simulations by adopting the constant opacities of $\kappa_{\text{gray}} \sim 0.1$–$20\,\text{cm}^2\,\text{g}^{-1}$ and compare the results with those with wavelength-dependent opacities.

The bolometric luminosity at $t < 1$ day for the model with the simple density structure and lanthanide-free abundances (model 3) can be reproduced by the gray transfer with the opacity $\kappa_{\text{gray}} \sim 0.8\,\text{cm}^2\,\text{g}^{-1}$ (Figure 14). This is because the outer layer opacity changes gradually at time $t < 1$ day, and hence, the behavior of the UVOIR transfer with the wavelength-dependent opacity can be simulated via UVOIR transfer with the gray opacity. However, for the similar models but with lanthanide-rich abundances (models 1 and 2), the luminosity cannot be well reproduced with a single gray opacity owing to the rapid changes in the opacity in the outer layer at $t < 1$ day. Similarly, for the models where the thin outer layer is present, the early luminosities cannot be reproduced (Figure 15).

The gray opacity might be a fair approximation to derive early luminosities if a range of the opacity values is considered instead of a single value. For example, take model 2, i.e., the simple model with the lanthanide-rich abundance for $Y_e = 0.20$–0.30. The UVOIR transfer with the gray opacity of $\kappa_{\text{gray}} \sim 5\,\text{cm}^2\,\text{g}^{-1}$ reproduces the faintest portion of the light
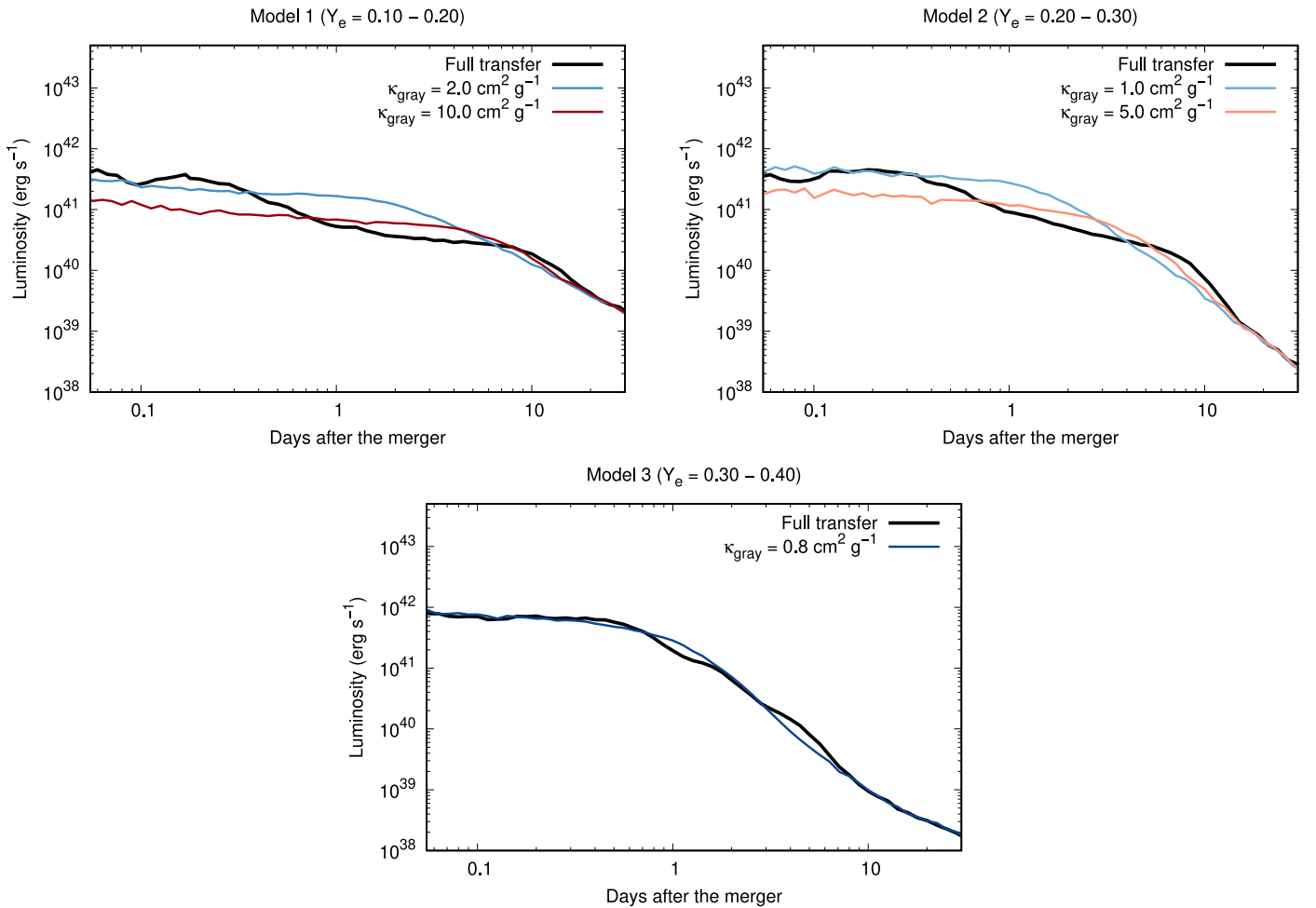
Figure 14. Bolometric light curves for the models with the single-density slope. The different panels represent different abundances in the thin outer layer. The light curves are compared with the light curves for the same model but with gray opacity.

curves at $t \sim 0.05$ day, whereas the brightest portion of the light curve around $t \sim 0.2$ day can be reproduced by the gray opacity of $\kappa_{\mathrm{gray}} \sim 1 \, \mathrm{cm}^2 \, \mathrm{g}^{-1}$. Similarly, the gray opacity equivalent for other models can be estimated. The results are summarized in Table 1. However, we want to stress the fact that the detailed trends of the light curves cannot be reproduced with a single gray opacity.

The multiband light curves cannot be reproduced by the UVOIR transfer with the gray opacity, even if the bolometric luminosities show a good match. Take, for example, the bolometric and the multicolor light curves for model 3 with the simple density and the lanthanide-free abundances. Although the bolometric luminosity shows a good match with the light curves with the gray opacity of $\kappa_{\mathrm{gray}} \sim 0.8 \, \mathrm{cm}^2 \, \mathrm{g}^{-1}$ (Figure 14), the multicolor light curves do not match (Figure 16). Hence, using the wavelength-dependent opacity is necessary to explain the multiband light curves from the observations.

Note that even though the opacity for the lanthanide-rich ejecta shows an extremely high value at far-UV wavelengths, the gray opacities required to reproduce the light curves at early time are not very high. This is because of the rapid evolution of the spectral peak toward the longer wavelengths due to temperature evolution in the outer layer ejecta. Hence, the gray opacities reproducing the light curves resemble the wavelength-dependent opacity at longer wavelengths, which are not very high.

5. Conclusions

To investigate the early kilonova emission from the neutron star merger ejecta, we perform the atomic opacity calculation for all the elements from La to Ra ($Z = 57$–88) ionized to the states V–XI, which are the typical conditions at $t = 0.1$ day (with $T \sim 10^5$ K). This work, together with previous work by Banerjee et al. (2020, 2022), provides the atomic opacities suitable at early time for all the elements from Ca to Ra ($Z = 20$–88) ionized from V to XI.

Our results show that the opacity varies widely depending on the existing open shell in the ions (Figure 4). For instance, the opacities for the lanthanides are exceptionally high, reaching $\kappa_{\mathrm{exp}} \sim 3 \times 10^3 \, \mathrm{cm}^2 \, \mathrm{g}^{-1}$ at the far-UV ($\lambda \leqslant 1000 \, \mathrm{\AA}$) at ionizations $\geqslant$ VII (Figure 2). Similarly, the opacities for the elements with open d-, p-, and s-shells reach $\kappa_{\mathrm{exp}} \sim 1$, 0.1, and 0.01 $\mathrm{cm}^2 \, \mathrm{g}^{-1}$, respectively, at the same wavelength range (Figure 4).

Using the new opacity data set, we perform radiative transfer simulations to derive the early kilonova light curves using a 1D spherical ejecta model with a power-law density structure. In neutron star mergers, the heaviest elements, including lanthanides, are expected to be distributed near the equatorial plane, whereas lighter r-process elements are distributed toward the pole or more isotropically. Because of the different elemental abundances, the opacity is different in different components, introducing the viewing angle dependence in the kilonova light
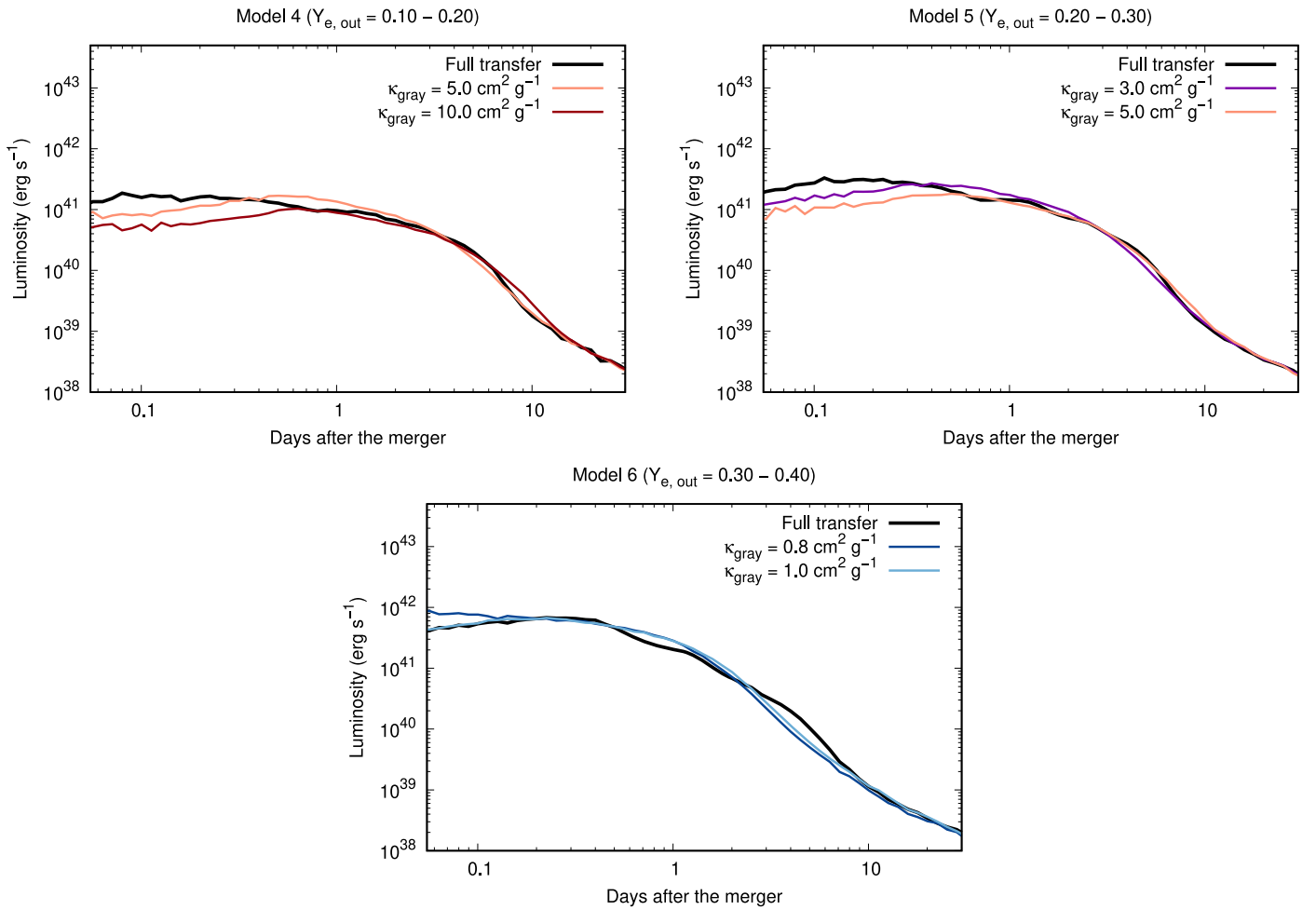
Figure 15. Bolometric light curves for the models with the thin outer layer with steeply declining density slope. The different panels represent different abundances in the thin outer layer. The light curves are compared with those for the same model but with the UVOIR transfer with gray opacity.

curves. To understand the light curves from polar and equatorial directions, we assume lanthanide-free and lanthanide-rich abundance of the ejecta, respectively. Furthermore, we study the effect of a faster moving thin outer layer with different compositions.

We find that in the presence of lanthanides in the ejecta, the bolometric luminosities ($L_{bol} \sim 3\text{--}4 \times 10^{41}$ erg s^{-1} is higher for the lower lanthanide fraction in the ejecta, e.g., model 2) are fainter in comparison with the bolometric luminosities for lanthanide-free ejecta ($L_{bol} \sim 8 \times 10^{41}$ erg s^{-1}, Figure 10). For the lanthanide-rich ejecta, there are distinct signatures in the early light curves determined by the evolution of the opacity in the outermost layer of the ejecta (Figure 11). Furthermore, the presence of a thin outer layer suppresses the early luminosity, in agreement with the results of Kasen et al. (2017) and Banerjee et al. (2020).

The UV brightness for a source at 100 Mpc at early time varies from ∼22–19.5 mag, fainter for the lanthanide-rich ejecta, at $t \sim 0.1$ day in the Swift UVOT filters (Roming et al. 2005). If the kilonova is discovered early enough so that the observation can be started promptly, then the UV signals can be detected with the existing Swift satellite (with a limiting magnitude of ∼22 mag for an exposure time of 1000 s, Roming et al. 2005), or the upcoming UV satellites, such as ULTRASAT (limiting magnitude of 22.4 mag for 900 s of integration time, Sagiv et al. 2014), Dorado (limiting

magnitude of 20.5 mag for 600 s of integration time, Dorsman et al. 2023), and UVEX (limiting magnitude of 25 mag for 900 s of integration time, Kulkarni et al. 2021).

The luminosities in the four optical filters (g, r, i, z bands) appear to vary from ∼21–20 mag at $t \sim 0.1$ day for a source at 100 Mpc. The light curves are fainter for the lanthanide-rich models, as in the bolometric luminosities. Moreover, the presence of the thin outer layers makes the light curves even fainter. For the optical g, r, i, z filters, the kilonovae for the lanthanide-rich ejecta are comparable to the detection limit of existing observing facilities such ZTF (Dekany et al. 2020). However, such kilonova might be detectable by the facilities with deeper observation limits, such as DECam (Chase et al. 2022) and Subaru-HSC (e.g., Ohgami et al. 2021, 2023). More interestingly, such kilonovae are good targets for upcoming wide-field surveys such as the Vera Rubin Observatory (Chase et al. 2022).

Finally we mention the limitations in our simulations. Our opacity in the far-UV wavelengths ($\lambda \leqslant 1000$ Å) may be underestimated, and hence, our light curves are possibly affected in the far-UV for lanthanide-rich models. However, the light curves in the longer wavelengths are likely to be unaffected by this choice since the detection ranges of the existing instruments are all beyond 2000 Å (e.g., Swift, Roming, et al. 2005; ZTF, Dekany et al. 2020). Furthermore, our 1D models are relatively simple. The effect of the more
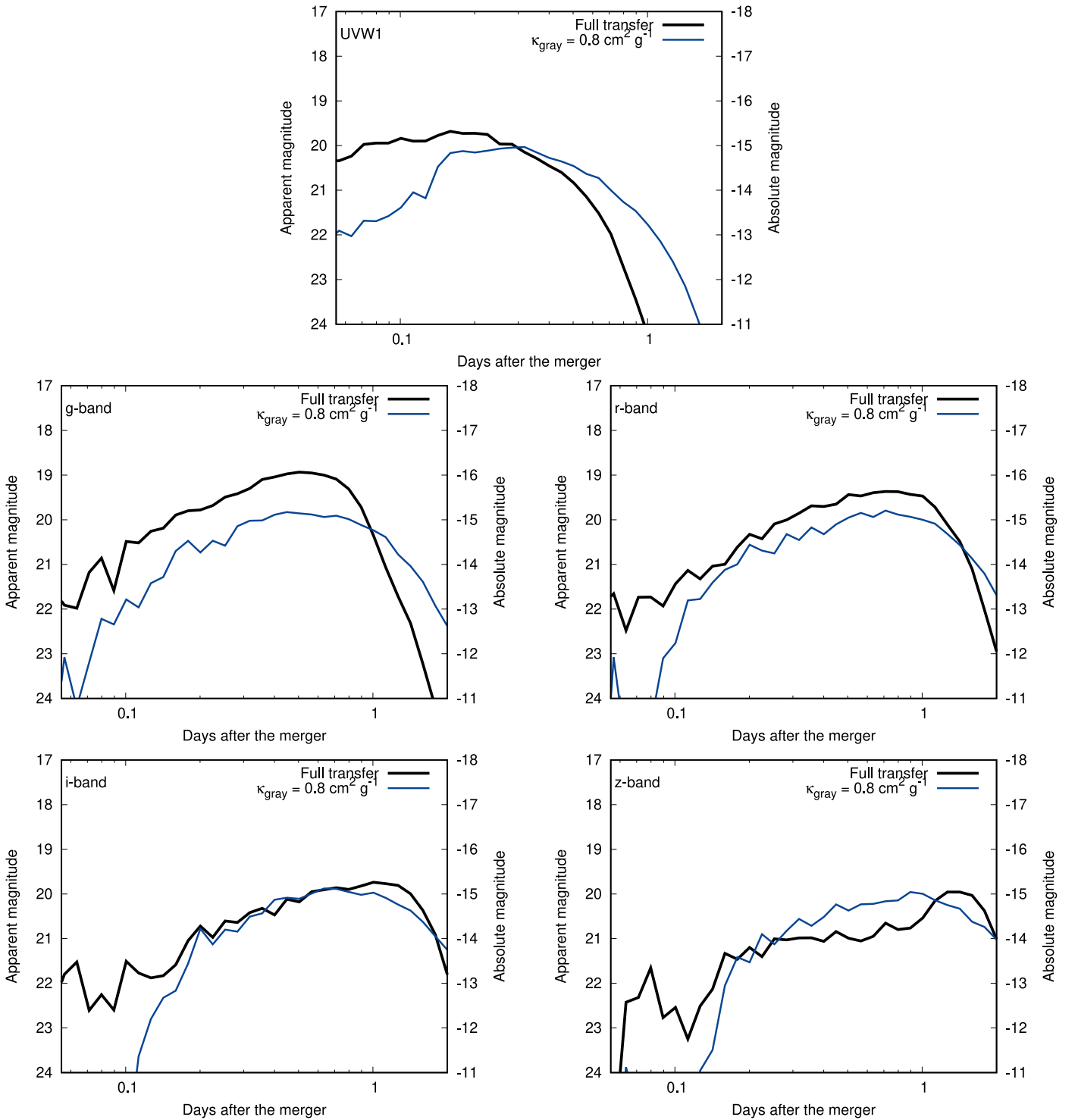
Figure 16. Comparison between the magnitudes in the Swift filter UVW1 (Roming et al. 2005) and the four optical filters in the *g*, *r*, *i*, *z* bands for the calculations assuming the UVOIR transfer with multiwavelength opacities (black) and the gray opacities (blue) for model 3, i.e., the model with the simple density and the lanthanide-free abundances. The source is assumed to be at a distance of 100 Mpc. The multicolor light curves cannot be reproduced with those from the UVOIR transfer calculations with the gray opacity.

realistic multidimensional ejecta structure will be explored in an upcoming work.

Appendix A
Effect of Choice of Partition Function on Opacity Calculation

In this section, we study the effect of choice of the approximated partition function on the opacity. For this purpose, we take the examples of light r-process ion Cd ($Z = 48$) IX and the lanthanide ion Eu ($Z = 63$) IX. In our previous studies (Banerjee et al. 2020, 2022), we adopted an approximated partition function by summing up the statistical weights up to a certain energy level, which is not dependent on the temperature. This choice of partition function gives a sound approximation for relatively simple elements but is not ideal for highly ionized lanthanides because of the closely spaced dense energy level structure, which can be easily populated. To demonstrate the effects of the choice of the partition function on the opacity, we show the wavelength-dependent expansion opacities for Cd IX and Eu IX at temperatures $T \sim 67{,}000$ and $\sim 64{,}000$ K (the temperatures at which the peaks of the IX ionizations are observed for Cd and Eu) in Figure A1 (left panel). The expansion opacity for Cd IX is not significantly affected by using the temperature-independent partition function taking selected energy levels (the dashed curve in the top left panel in Figure A1). However, the same is not true for Eu IX, as the expansion opacity is affected by the choice (the dashed curve in the bottom left panel in Figure A1). The same trend is also observed in the Planck mean opacities (right panel in Figure A1) for Cd IX and Eu IX.
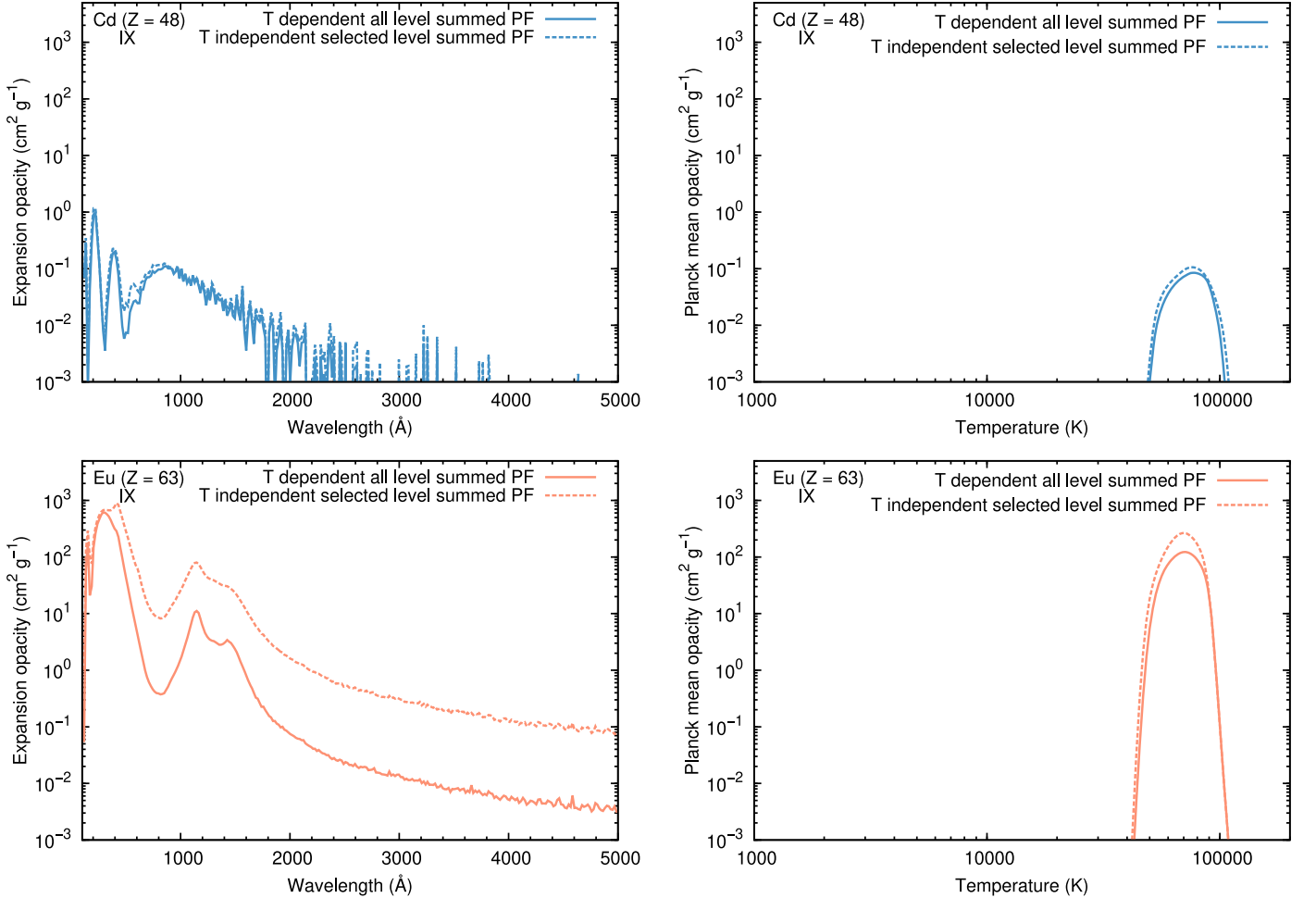
Figure A1. Left: the expansion opacity as a function of wavelength. Right: Planck mean opacity as a function of temperature for Cd IX (top) and Eu IX (bottom). The wavelength-dependent opacities for the Cd and Eu are shown at temperatures $T \sim 67{,}000$ and $\sim 64{,}000$ K. These are the temperatures around which the peaks of the IX ionizations are observed for Cd and Eu. The solid and the dashed curves are calculated using temperature-dependent and independent partition functions, respectively. The differences in the expansion opacities are insignificant for Cd IX with a relatively simple energy level structure; however, the deviations are observed for Eu IX with densely spaced energy levels.

Appendix B
Configurations Used for the Calculations

We show all the configurations used in our work in Table B1.

Table B1
Configurations and the Results from the Atomic Structure Calculations

Ion	Configurations	N_{level}	N_{line}	N_{line}^*
La V	$\mathbf{5p^5}$, $5p^44f^1$, $5p^46s^1$, $5p^45d^1$, $5p^46p^1$	89	1124	1124
La VI	$\mathbf{5p^4}$, $5p^34f^1$, $5p^36s^1$, $5p^35d^1$, $5p^36p^1$	121	1937	1937
La VII	$\mathbf{5p^3}$, $5p^24f^1$, $5p^26s^1$, $5p^25d^1$, $5p^26p^1$	92	1208	1208
La VIII	$\mathbf{5p^2}$, $5p^14f^1$, $5p^16s^1$, $5p^15d^1$, $5p^16p^1$	43	254	254
La IX	$\mathbf{5p^1}5s^2$, $5p^15s^14f^1$, $5p^15s^16s^1$, $5p^15s^15d^1$,$5p^15s^16p^1$	74	808	808
La X	$\mathbf{5s^2}$, $5s^14f^1$, $5s^16s^1$, $5s^15d^1$, $5s^16p^1$	15	30	30
La XI	$\mathbf{5s^1}4d^{10}$, $4d^{10}4f^1$, $4d^{10}6s^1$, $4d^{10}5d^1$,$4d^{10}6p^1$	8	10	10
Ce V	$\mathbf{5p^6}$, $4f^25p^4$, $4f^15p^5$, $5p^56s^1$, $5p^56p^1$, $5p^55d^1$	210	1274	1274
Ce VI	$\mathbf{5p^5}$, $4f^25p^3$, $4f^15p^4$, $5p^46s^1$, $5p^46p^1$, $5p^45d^1$	310	4420	4420
Ce VII	$\mathbf{5p^4}$, $4f^25p^2$, $4f^15p^3$, $5p^36s^1$, $5p^36p^1$, $5p^35d^1$	292	5233	5233
Ce VIII	$\mathbf{5p^3}$, $4f^25p^1$, $4f^15p^2$, $5p^26s^1$, $5p^26p^1$, $5p^25d^1$	161	2271	2271
Ce IX	$\mathbf{5p^2}$, $4f^15p^1$, $5p^16s^1$, $5p^16p^1$, $5p^15d^1$, $5p^17s^1$	47	315	315
Ce X	$\mathbf{5p^1}4d^{10}$, $4d^{10}7s^1$, $4d^{10}4f^1$, $4d^{10}6s^1$, $4d^{10}6p^1$, $4d^{10}5d^1$	10	17	17
Ce XI	$\mathbf{4d^{10}}5s^2$, $4d^{10}5s^17s^1$, $4d^{10}5s^14f^1$, $4d^{10}5s^16s^1$,$4d^{10}5s^16p^1$, $4d^{10}5s^15d^1$	17	36	36
Pr V	$\mathbf{4f^1}5p^6$, $5p^67s^1$, $5p^67p^1$, $5p^66s^1$, $5p^66p^1$, $5p^65d^1$	10	17	17
Pr VI	$\mathbf{5p^6}$, $5p^54f^1$, $5p^57p^1$, $5p^56s^1$, $5p^56p^1$, $5p^55d^1$	49	317	317
Pr VII	$\mathbf{5p^5}$, $5p^44f^1$, $5p^47p^1$, $5p^46s^1$, $5p^46p^1$, $5p^45d^1$	110	1634	1634
Pr VIII	$\mathbf{5p^4}$, $5p^34f^1$, $5p^37p^1$, $5p^36s^1$, $5p^36p^1$, $5p^35d^1$	149	2771	2771
Pr IX	$\mathbf{5p^3}$, $5p^24f^1$, $5p^27p^1$, $5p^26s^1$, $5p^26p^1$, $5p^25d^1$	113	1718	1718
Pr X	$\mathbf{5p^2}$, $4f^2$, $5p^14f^1$, $5p^16s^1$, $5p^16p^1$, $5p^15d^1$	56	337	337
Pr XI	$\mathbf{5p^1}5s^2$, $5s^24f^1$, $5s^27p^1$, $5s^26s^1$, $5s^26p^1$,$5s^25d^1$	11	18	18
Nd V	$\mathbf{4f^2}5p^6$, $4f^35p^5$, $4f^15p^67p^1$, $4f^15p^66s^1$,$4f^15p^66p^1$, $4f^15p^65d^1$	303	2811	2811
Nd VI	$\mathbf{4f^1}5p^6$, $4f^25p^5$, $5p^67p^1$, $5p^66s^1$, $5p^66p^1$, $5p^65d^1$	78	96	96
Nd VII	$\mathbf{5p^6}$, $5p^44f^2$, $5p^54f^1$, $5p^56s^1$, $5p^56p^1$, $5p^55d^1$	210	1274	1274
Nd VIII	$\mathbf{5p^5}$, $4f^15p^4$, $4f^25p^3$, $4f^15p^36s^1$, $4f^15p^36p^1$, $4f^15p^35d^1$	926	96,706	96,706
Nd IX	$\mathbf{4f^1}5p^3$, $5p^4$, $5p^24f^2$, $4f^15p^26s^1$, $4f^15p^26p^1$, $4f^15p^25d^1$	730	59,206	59,206
Nd X	$\mathbf{4f^1}5p^2$, $5p^3$, $4f^25p^1$, $4f^15p^16s^1$, $4f^15p^16p^1$, $4f^15p^15d^1$	312	11,561	11,561
Nd XI	$\mathbf{5p^1}4f^1$, $5p^2$, $4f^2$, $5p^16s^1$, $5p^16p^1$, $5p^15d^1$	56	337	337
Pm V	$\mathbf{4f^3}5p^6$, $4f^45p^5$, $4f^35p^55d^1$, $4f^35p^56s^1$, $4f^35p^56p^1$, $4f^35p^57p^1$, $4f^35p^57s^1$, $4f^35p^56d^1$	8856	6,533,898	6,036,921
Pm VI	$\mathbf{4f^2}5p^6$, $4f^35p^5$, $4f^25p^55d^1$, $4f^25p^56s^1$, $4f^25p^56p^1$, $4f^25p^57p^1$, $4f^25p^57s^1$, $4f^25p^56d^1$	2583	613,722	613,722
Pm VII	$\mathbf{4f^2}5p^5$, $4f^35p^4$, $4f^25p^45d^1$, $4f^25p^46s^1$, $4f^25p^46p^1$, $4f^25p^47p^1$, $4f^25p^47s^1$, $4f^25p^46d^1$	6286	3,647,090	3,647,090
Pm VIII	$\mathbf{4f^2}5p^4$, $4f^35p^3$, $4f^25p^35d^1$, $4f^25p^36s^1$, $4f^25p^36p^1$, $4f^25p^37p^1$, $4f^25p^37s^1$, $4f^25p^36d^1$	8479	6,488,816	6,488,816
Pm IX	$\mathbf{4f^2}5p^3$, $4f^35p^2$, $4f^25p^25d^1$, $4f^25p^26s^1$, $4f^25p^26p^1$, $4f^25p^27p^1$, $4f^25p^27s^1$, $4f^25p^26d^1$	6438	3,865,322	3,865,322
Pm X	$\mathbf{4f^2}5p^2$, $4f^35p^1$, $4f^25p^15d^1$, $4f^25p^16s^1$, $4f^25p^16p^1$, $4f^25p^17p^1$, $4f^25p^17s^1$, $4f^25p^16d^1$	2741	706,348	706,348
Pm XI	$\mathbf{4f^2}5p^1$, $4f^3$, $4f^25d^1$, $4f^26s^1$, $4f^26p^1$, $4f^27p^1$, $4f^27s^1$, $4f^26d^1$	510	26,228	26,228
Sm V	$\mathbf{4f^4}5p^6$, $4f^55p^5$, $4f^35p^66s^1$, $4f^35p^66p^1$, $4f^35p^65d^1$, $4f^35p^67s^1$	2067	283,093	283,093
Sm VI	$\mathbf{4f^3}5p^6$, $4f^45p^5$, $4f^35p^56s^1$, $4f^35p^56p^1$, $4f^35p^55d^1$, $4f^35p^57s^1$	5230	2,288,568	2,288,568
Sm VII	$\mathbf{4f^3}5p^5$, $4f^25p^6$, $4f^35p^46s^1$, $4f^35p^46p^1$, $4f^35p^45d^1$, $4f^35p^47s^1$	11,589	9,998,002	9,998,002
Sm VIII	$\mathbf{4f^3}5p^4$, $4f^25p^5$, $4f^35p^36s^1$, $4f^35p^36p^1$, $4f^35p^35d^1$, $4f^35p^37s^1$	15,567	18,619,221	18,619,221
Sm IX	$\mathbf{4f^3}5p^3$, $4f^25p^4$, $4f^35p^26s^1$, $4f^35p^26p^1$, $4f^35p^25d^1$, $4f^35p^27s^1$	12,293	11,835,344	11,835,344
Sm X	$\mathbf{4f^3}5p^2$, $4f^25p^3$, $4f^35p^16s^1$, $4f^35p^16p^1$, $4f^35p^15d^1$, $4f^35p^17s^1$	5388	2,497,192	2,497,192
Sm XI	$\mathbf{4f^3}5p^1$, $4f^25p^2$, $4f^36s^1$, $4f^36p^1$, $4f^35d^1$, $4f^37s^1$	1205	130,432	130,432
Eu V	$\mathbf{4f^5}5p^6$, $4f^65p^5$, $4f^45p^66s^1$, $4f^45p^66p^1$, $4f^45p^65d^1$, $4f^45p^67s^1$	3897	1,140,035	1,137,991
Eu VI	$\mathbf{4f^4}5p^6$, $4f^55p^5$, $4f^45p^56s^1$, $4f^45p^56p^1$, $4f^45p^55d^1$, $4f^45p^57s^1$	13,065	12,823,350	12,819,025
Eu VII	$\mathbf{4f^4}5p^5$, $4f^35p^6$, $4f^45p^46s^1$, $4f^45p^46p^1$, $4f^45p^45d^1$, $4f^45p^47s^1$	29,465	60,643,899	60,636,013
Eu VIII	$\mathbf{4f^4}5p^4$, $4f^35p^5$, $4f^45p^36s^1$, $4f^45p^36p^1$, $4f^45p^35d^1$, $4f^45p^37s^1$	40,241	113,753,012	113,745,357
Eu IX	$\mathbf{4f^4}5p^3$, $4f^35p^4$, $4f^45p^26s^1$, $4f^45p^26p^1$, $4f^45p^25d^1$, $4f^45p^27s^1$	31,393	73,355,941	73,355,941
Eu X	$\mathbf{4f^4}5p^2$, $4f^35p^3$, $4f^35p^26s^1$, $4f^45p^16s^1$, $4f^45p^16p^1$, $4f^45p^15d^1$, $4f^45p^17s^1$	15,515	18,807,502	18,787,178
Eu XI	$\mathbf{4f^4}5p^1$, $4f^35p^2$, $4f^46s^1$, $4f^46p^1$, $4f^45d^1$, $4f^47s^1$	3204	853,861	853,861
Gd V	$\mathbf{4f^6}5p^6$, $4f^75p^5$, $4f^55p^65d^1$, $4f^55p^66s^1$, $4f^55p^66p^1$	5665	2,403,983	2,403,983
Gd VI	$\mathbf{4f^5}5p^6$, $4f^65p^5$, $4f^55p^55d^1$, $4f^55p^56s^1$, $4f^55p^56p^1$	21,926	35,616,475	35,616,475
Gd VII	$\mathbf{4f^5}5p^5$, $4f^45p^6$, $4f^55p^45d^1$, $4f^55p^46s^1$, $4f^55p^46p^1$	50,969	180,288,431	180,288,431

Table B1
(Continued)

Ion	Configurations	N_{level}	N_{line}	N_{line}^{*}
Gd VIII	$\mathbf{4f^5 5p^4}$, $\mathbf{4f^4 5p^5}$, $4f^6 5p^3$, $4f^5 5p^3 6s^1$, $4f^5 5p^3 6p^1$	38,760	73,593,381	73,593,381
Gd IX	$\mathbf{4f^5 5p^3}$, $4f^4 5p^4$, $4f^5 5p^2 5d^1$, $4f^5 5p^2 6s^1$, $4f^5 5p^2 6p^1$	55 029	220,240,570	220,240,570
Gd X	$\mathbf{4f^4 5p^3}$, $4f^5 5p^2$, $4f^5 5p^1 5d^1$, $4f^5 5p^1 6s^1$, $4f^5 5p^1 6p^1$, $4f^5 5p^1 7s^1$	27,187	55,999,215	55,999,215
Gd XI	$\mathbf{4f^5 5p^1}$, $4f^4 5p^2$, $4f^5 5d^1$, $4f^5 6s^1$, $4f^5 6p^1$, $4f^3 5p^3$	6915	3,359,449	3,359,449
Tb V	$\mathbf{4f^7 5p^6}$, $\mathbf{4f^8 5p^5}$, $4f^6 5p^6 5d^1$, $4f^6 5p^6 6s^1$, $4f^6 5p^6 6p^1$, $4f^6 5p^6 6d^1$, $4f^6 5p^6 7s^1$, $4f^6 5p^6 7p^1$, $4f^9 5p^4$	14,872	16,965,765	13,717,001
Tb VI	$\mathbf{4f^6 5p^6}$, $\mathbf{4f^7 5p^5}$, $4f^6 5p^6 5d^1$, $4f^6 5p^6 6s^1$, $4f^6 5p^6 6p^1$, $4f^6 5p^6 6d^1$, $4f^6 5p^6 7s^1$, $4f^6 5p^6 7p^1$, $4f^8 5p^4$	65,376	308,013,551	292,972,426
Tb VII	$\mathbf{4f^6 5p^5}$, $\mathbf{4f^7 5p^4}$, $4f^6 5p^4 5d^1$, $4f^6 5p^4 6s^1$, $4f^6 5p^4 6p^1$, $4f^6 5p^4 7p^1$	103,141	783,718,762	770,562,843
Tb VIII	$\mathbf{4f^6 5p^4}$, $\mathbf{4f^8 5p^5}$, $4f^6 5p^3 5d^1$, $4f^6 5p^3 6s^1$, $4f^6 5p^3 6p^1$, $4f^7 5p^3$	108,155	827,860,706	82,782,424
Tb IX	$\mathbf{4f^6 5p^3}$, $\mathbf{4f^8 5p^4}$, $4f^6 5p^2 5d^1$, $4f^6 5p^2 6s^1$, $4f^6 5p^2 6p^1$, $4f^7 5p^2$	85,367	529,201,954	52,910,542
Tb X	$\mathbf{4f^6 5p^2}$, $\mathbf{4f^8 5p^3}$, $4f^6 5p^1 5d^1$, $4f^6 5p^1 6s^1$, $4f^6 5p^1 6p^1$, $4f^6 5p^1 7p^1$, $4f^6 5p^1 7s^1$, $4f^6 5p^1 6d^1$, $4f^7 5p^1$	68,899	347,094,944	34,706,673
Tb XI	$\mathbf{4f^6 5p^1}$, $\mathbf{4f^8 5p^2}$, $4f^6 5d^1$, $4f^6 6s^1$, $4f^6 6p^1$, $4f^6 7p^1$, $4f^6 7s^1$, $4f^6 6d^1$, $4f^7$	14,872	16,982,008	1,698,216
Dy V	$\mathbf{4f^8 5p^6}$, $\mathbf{4f^9 5p^5}$, $4f^8 5p^5 6s^1$, $4f^8 5p^5 6p^1$, $4f^8 5p^5 5d^1$, $4f^8 5p^5 7s^1$, $4f^8 5p^5 7p^1$, $4f^8 5p^5 6d^1$, $4f^{10} 5p^4$	61,924	268,129,383	80,876,994
Dy VI	$\mathbf{4f^7 5p^6}$, $\mathbf{4f^8 5p^5}$, $4f^7 5p^5 5d^1$, $4f^7 5p^5 6s^1$, $4f^7 5p^5 6p^1$, $4f^7 5p^5 7s^1$, $4f^7 5p^5 7p^1$, $4f^7 5p^5 6d^1$, $4f^9 5p^4$	71,234	360,956,051	327,573,289
Dy VII	$\mathbf{4f^7 5p^5}$, $\mathbf{4f^6 5p^6}$, $4f^7 5p^4 5d^1$, $4f^7 5p^4 6p^1$, $4f^7 5p^4 6s^1$, $4f^7 5p^4 7s^1$	94 015	566,376,534	56,332,605
Dy VIII	$\mathbf{4f^7 5p^4}$, $\mathbf{4f^6 5p^5}$, $4f^7 5p^3 5d^1$, $4f^7 5p^3 6s^1$, $4f^7 5p^3 6p^1$	115,103	913,738,089	913,738,089
Dy IX	$\mathbf{4f^7 5p^3}$, $\mathbf{4f^6 5p^4}$, $4f^7 5p^2 6s^1$, $4f^7 5p^2 6p^1$, $4f^7 5p^2 5d^1$	92,861	610,943,987	61,108,625
Dy X	$\mathbf{4f^7 5p^2}$, $\mathbf{4f^6 5p^3}$, $4f^7 5p^1 6s^1$, $4f^7 5p^1 6p^1$, $4f^7 5p^1 5d^1$, $4f^7 5p^1 7s^1$, $4f^7 5p^1 7p^1$, $4f^7 5p^1 6d^1$, $4f^8 5p^1$	78,312	447,640,090	44,771,955
Dy XI	$\mathbf{4f^7 5p^1}$, $\mathbf{4f^6 5p^2}$, $4f^7 6s^1$, $4f^7 6p^1$, $4f^7 5d^1$, $4f^7 7s^1$, $4f^7 7p^1$, $4f^7 6d^1$, $4f^8$	17,808	23,445,375	2,345,926
Ho V	$\mathbf{4f^9 5p^6}$, $\mathbf{4f^{10} 5p^5}$, $4f^8 5p^5 6s^1$, $4f^8 5p^5 6p^1$, $4f^8 5p^5 5d^1$, $4f^8 5p^5 7s^1$, $4f^8 5p^5 7p^1$, $4f^8 5p^5 6d^1$, $4f^{11} 5p^4$	11,390	9,922,122	7,864,433
Ho VI	$\mathbf{4f^8 5p^6}$, $\mathbf{4f^9 5p^5}$, $4f^8 5p^5 6s^1$, $4f^8 5p^5 6p^1$, $4f^8 5p^5 5d^1$, $4f^8 5p^5 7s^1$, $4f^8 5p^5 7p^1$, $4f^8 5p^5 6d^1$, $4f^{10} 5p^4$	61,924	268,129,383	256,960,118
Ho VII	$\mathbf{4f^7 5p^6}$, $\mathbf{4f^8 5p^5}$, $4f^7 5p^5 6s^1$, $4f^7 5p^5 6p^1$, $4f^7 5p^5 5d^1$, $4f^7 5p^5 7s^1$, $4f^7 5p^5 7p^1$, $4f^7 5p^5 6d^1$, $4f^9 5p^4$	71,234	360,956,050	348,425,416
Ho VIII	$\mathbf{4f^7 5p^5}$, $\mathbf{4f^6 5p^6}$, $4f^7 5p^4 5d^1$, $4f^7 5p^4 6s^1$, $4f^7 5p^4 6p^1$	84 567	481 201 997	48 111 620
Ho IX	$\mathbf{4f^7 5p^4}$, $\mathbf{4f^6 5p^5}$, $4f^7 5p^3 5d^1$, $4f^7 5p^3 6s^1$, $4f^7 5p^3 6p^1$	115,103	913,738,088	913,738,088
Ho X	$\mathbf{4f^7 5p^3}$, $\mathbf{4f^6 5p^4}$, $4f^7 5p^2 5d^1$, $4f^7 5p^2 6s^1$, $4f^7 5p^2 6p^1$, $4f^5 5p^5$	94,029	629,847,851	62,984,708
Ho XI	$\mathbf{4f^7 5p^2}$, $\mathbf{4f^6 5p^3}$, $4f^7 5p^1 5d^1$, $4f^7 5p^1 6s^1$, $4f^7 5p^1 6p^1$, $4f^7 5p^1 6d^1$, $4f^7 5p^1 7s^1$, $4f^7 5p^1 7p^1$, $4f^8 5p^1$	78,312	447,640,089	44,755,094
Er V	$\mathbf{4f^{10} 5p^6}$, $\mathbf{4f^{11} 5p^5}$, $4f^9 5p^6 5d^1$, $4f^9 5p^6 6s^1$, $4f^9 5p^6 6p^1$, $4f^9 5p^6 7s^1$, $4f^9 5p^6 7p^1$, $4f^9 5p^6 6d^1$, $4f^{12} 5p^4$	7404	4,126,324	3,500,857
Er VI	$\mathbf{4f^9 5p^6}$, $\mathbf{4f^{10} 5p^5}$, $4f^8 5p^6 5d^1$, $4f^8 5p^6 6s^1$, $4f^8 5p^6 6p^1$, $4f^8 5p^6 7s^1$, $4f^8 5p^6 7p^1$, $4f^8 5p^6 6d^1$, $4f^{11} 5p^4$	11,390	9,922,122	9,829,677
Er VII	$\mathbf{4f^8 5p^6}$, $\mathbf{4f^9 5p^5}$, $4f^8 5p^5 5d^1$, $4f^8 5p^5 6s^1$, $4f^8 5p^5 6p^1$, $4f^8 5p^5 7s^1$, $4f^8 5p^5 7p^1$, $4f^8 5p^5 6d^1$, $4f^{10} 5p^4$	61,924	268,129,380	264,770,945
Er VIII	$\mathbf{4f^8 5p^5}$, $\mathbf{4f^7 5p^6}$, $4f^8 5p^4 5d^1$, $4f^8 5p^4 6s^1$, $4f^8 5p^4 6p^1$, $4f^9 5p^4$	77,126	419,766,790	41,973,419
Er IX	$\mathbf{4f^8 5p^4}$, $\mathbf{4f^7 5p^5}$, $4f^8 5p^3 5d^1$, $4f^8 5p^3 6s^1$, $4f^8 5p^3 6p^1$, $4f^9 5p^3$	106,425	793,905,120	793,905,120
Er X	$\mathbf{4f^8 5p^3}$, $4f^7 5p^4$, $4f^8 5p^2 5d^1$, $4f^8 5p^2 6s^1$, $4f^8 5p^2 6p^1$, $4f^8 5p^2 7s^1$, $4f^8 5p^2 7p^1$	115,282	960,990,869	96,106,686
Er XI	$\mathbf{4f^8 5p^2}$, $4f^7 5p^3$, $4f^8 5p^1 5d^1$, $4f^8 5p^1 6s^1$, $4f^8 5p^1 6p^1$, $4f^8 5p^1 7s^1$, $4f^8 5p^1 7p^1$, $4f^8 5p^1 6d^1$, $4f^9 5p^1$	70,629	369,445,987	36,941,739
Tm V	$\mathbf{4f^{11} 5p^6}$, $\mathbf{4f^{12} 5p^5}$, $4f^{10} 5p^6 5d^1$, $4f^{10} 5p^6 6s^1$, $4f^{10} 5p^6 6p^1$, $4f^{10} 5p^6 7s^1$, $4f^{10} 5p^6 7p^1$, $4f^{10} 5p^6 6d^1$, $4f^{13} 5p^4$	3732	1,089,456	1,000,581
Tm VI	$\mathbf{4f^{10} 5p^6}$, $\mathbf{4f^{11} 5p^5}$, $4f^9 5p^6 5d^1$, $4f^9 5p^6 6s^1$, $4f^9 5p^6 6p^1$, $4f^9 5p^6 7s^1$, $4f^9 5p^6 7p^1$, $4f^9 5p^6 6d^1$, $4f^{12} 5p^4$	7404	4,126,324	4,106,920
Tm VII	$\mathbf{4f^9 5p^6}$, $\mathbf{4f^{10} 5p^5}$, $4f^9 5p^5 5d^1$, $4f^9 5p^5 6s^1$, $4f^9 5p^5 6p^1$, $4f^9 5p^5 7s^1$, $4f^9 5p^5 7p^1$, $4f^9 5p^5 6d^1$, $4f^{11} 5p^4$	41,464	123,981,375	123,401,551
Tm VIII	$\mathbf{4f^9 5p^5}$, $\mathbf{4f^8 5p^6}$, $4f^9 5p^4 5d^1$, $4f^9 5p^4 6s^1$, $4f^9 5p^4 6p^1$, $4f^9 5p^4 7s^1$, $4f^9 5p^4 7p^1$, $4f^9 5p^4 6d^1$, $4f^{10} 5p^4$	102,368	725,210,231	721,396,552
Tm IX	$\mathbf{4f^9 5p^4}$, $\mathbf{4f^8 5p^5}$, $4f^9 5p^3 6s^1$, $4f^9 5p^3 6p^1$, $4f^9 5p^3 5d^1$	70,095	351,045,169	35,103,643
Tm X	$\mathbf{4f^9 5p^3}$, $\mathbf{4f^8 5p^4}$, $4f^9 5p^2 5d^1$, $4f^9 5p^2 6s^1$, $4f^9 5p^2 6p^1$, $4f^9 5p^2 7s^1$, $4f^9 5p^2 7p^1$, $4f^9 5p^2 6d^1$, $4f^{10} 5p^2$	108,932	853,007,622	853,007,622
Tm XI	$\mathbf{4f^9 5p^2}$, $\mathbf{4f^8 5p^3}$, $4f^9 5p^1 5d^1$, $4f^9 5p^1 6s^1$, $4f^9 5p^1 6p^1$, $4f^9 5p^1 7s^1$, $4f^9 5p^1 7p^1$, $4f^9 5p^1 6d^1$, $4f^{10} 5p^1$	49,074	184,983,546	184,983,546
Yb V	$\mathbf{4f^{12} 5p^6}$, $4f^{13} 5p^5$, $4f^{11} 5p^6 5d^1$, $4f^{11} 5p^6 6s^1$, $4f^{11} 5p^6 6p^1$, $4f^{11} 5p^6 7s^1$	817	53,275	53,275
Yb VI	$\mathbf{4f^{11} 5p^6}$, $4f^{12} 5p^5$, $4f^{10} 5p^6 5d^1$, $4f^{10} 5p^6 6s^1$, $4f^{10} 5p^6 6p^1$, $4f^{10} 5p^6 7s^1$	2114	340,857	340,857
Yb VII	$\mathbf{4f^{10} 5p^6}$, $4f^{11} 5p^5$, $4f^{10} 5p^5 5d^1$, $4f^{10} 5p^5 6s^1$, $4f^{10} 5p^5 6p^1$, $4f^{10} 5p^5 7s^1$	12,139	10,457,118	10,455,862
Yb VIII	$\mathbf{4f^{10} 5p^5}$, $4f^9 5p^6$, $4f^{10} 5p^4 5d^1$, $4f^{10} 5p^4 6s^1$, $4f^{10} 5p^4 6p^1$, $4f^{10} 5p^4 7s^1$	29,622	61,593,132	61,585,120
Yb IX	$\mathbf{4f^{10} 5p^4}$, $4f^9 5p^5$, $4f^{10} 5p^3 5d^1$, $4f^{10} 5p^3 6s^1$, $4f^{10} 5p^3 6p^1$, $4f^{10} 5p^3 7s^1$	41,167	121,033,516	121,033,516
Yb X	$\mathbf{4f^{10} 5p^3}$, $4f^9 5p^4$, $4f^{10} 5p^2 5d^1$, $4f^{10} 5p^2 6s^1$, $4f^{10} 5p^2 6p^1$, $4f^8 5p^5$	32,376	83,021,204	83,021,204
Yb XI	$\mathbf{4f^{10} 5p^2}$, $4f^9 5p^3$, $4f^{10} 5p^1 5d^1$, $4f^{10} 5p^1 6s^1$, $4f^{10} 5p^1 6p^1$, $4f^8 5p^4$	20,112	28,733,284	28,733,284
Lu V	$\mathbf{4f^{13} 5p^6}$, $4f^{14} 5p^5$, $4f^{12} 5p^6 5d^1$, $4f^{12} 5p^6 6s^1$, $4f^{12} 5p^6 6p^1$, $4f^{12} 5p^6 7s^1$	228	4611	4611
Lu VI	$\mathbf{4f^{12} 5p^6}$, $4f^{13} 5p^5$, $4f^{11} 5p^6 5d^1$, $4f^{11} 5p^6 6s^1$, $4f^{11} 5p^6 6p^1$, $4f^{11} 5p^6 7s^1$	817	53,275	53,275
Lu VII	$\mathbf{4f^{11} 5p^6}$, $4f^{12} 5p^5$, $4f^{11} 5p^5 5d^1$, $4f^{11} 5p^5 6s^1$, $4f^{11} 5p^5 6p^1$, $4f^{11} 5p^5 7s^1$	4688	1,700,280	1,700,280
Lu VIII	$\mathbf{4f^{11} 5p^5}$, $\mathbf{4f^{10} 5p^6}$, $4f^{11} 5p^4 5d^1$, $4f^{11} 5p^4 6s^1$, $4f^{11} 5p^4 6p^1$, $4f^{11} 5p^4 7s^1$	11,683	10,247,264	10,247,264
Lu IX	$\mathbf{4f^{11} 5p^4}$, $\mathbf{4f^{10} 5p^5}$, $4f^{11} 5p^3 5d^1$, $4f^{11} 5p^3 6s^1$, $4f^{11} 5p^3 6p^1$, $4f^{11} 5p^3 7s^1$	16,109	20,510,918	20,510,918
Lu X	$\mathbf{4f^{11} 5p^3}$, $4f^{10} 5p^4$, $4f^{11} 5p^2 5d^1$, $4f^{11} 5p^2 6s^1$, $4f^{11} 5p^2 6p^1$, $4f^{11} 5p^2 7s^1$	13,639	15,335,633	15,335,633
Lu XI	$\mathbf{4f^{11} 5p^2}$, $4f^{10} 5p^3$, $4f^{11} 5p^1 5d^1$, $4f^{11} 5p^1 6s^1$, $4f^{11} 5p^1 6p^1$, $4f^{11} 5p^1 7s^1$	7158	4,380,853	4 380,853
Hf V	$\mathbf{4f^{14} 5p^6}$, $4f^{12} 5p^6 6s^2$, $4f^{12} 5p^6 5d^2$, $4f^{12} 5p^6 6p^2$, $4f^{13} 5p^6 6s^1$, $4f^{13} 5p^6 5d^1$, $4f^{13} 5p^6 6p^1$, $4f^{14} 5p^5 6s^1$, $4f^{14} 5p^5 5d^1$, $4f^{14} 5p^5 6p^1$	704	10,461	7105
Hf VI	$\mathbf{4f^{13} 5p^6}$, $4f^{11} 5p^6 6s^2$, $4f^{11} 5p^6 5d^2$, $4f^{11} 5p^6 6p^2$, $4f^{12} 5p^6 6s^1$, $4f^{12} 5p^6 5d^1$, $4f^{12} 5p^6 6p^1$, $4f^{13} 5p^6 6s^1$, $4f^{13} 5p^5 5d^1$, $4f^{13} 5p^5 6p^1$	2668	240,950	174,990
Hf VII	$\mathbf{4f^{13} 5p^5}$, $4f^{11} 5p^5 6s^2$, $4f^{11} 5p^5 5d^2$, $4f^{11} 5p^5 6p^2$, $4f^{12} 5p^5 6s^1$, $4f^{12} 5p^5 5d^1$, $4f^{12} 5p^5 6p^1$, $4f^{13} 5p^4 6s^1$, $4f^{13} 5p^4 5d^1$, $4f^{13} 5p^4 6p^1$	14,972	5,370,715	3,874,607

Table B1
(Continued)

Ion	Configurations	N_{level}	N_{line}	N_{line}^*
Hf VIII	$\mathbf{4f^{13}5p^4}$, $4f^{11}5p^46s^2$, $4f^{11}5p^45d^2$, $4f^{11}5p^46p^2$, $4f^{12}5p^46s^1$, $4f^{12}5p^45d^1$, $4f^{12}5p^46p^1$, $4f^{13}5p^36s^1$, $4f^{13}5p^35d^1$, $4f^{13}5p^36p^1$	35,958	26,949,534	19,498,022
Hf IX	$\mathbf{4f^{13}5p^3}$, $4f^{11}5p^36s^2$, $4f^{11}5p^35d^2$, $4f^{11}5p^36p^2$, $4f^{12}5p^36s^1$, $4f^{12}5p^35d^1$, $4f^{12}5p^36p^1$, $4f^{13}5p^26s^1$, $4f^{13}5p^25d^1$, $4f^{13}5p^26p^1$	47,646	42,884,855	31,062,138
Hf X	$\mathbf{4f^{13}5p^2}$, $4f^{12}5p^16s^2$, $4f^{12}5p^15d^2$, $4f^{12}5p^16p^2$, $4f^{12}5p^26s^1$, $4f^{12}5p^25d^1$, $4f^{12}5p^26p^1$, $4f^{13}5p^16s^1$, $4f^{13}5p^15d^1$, $4f^{13}5p^16p^1$	6703	3,537,394	2,893,863
Hf XI	$\mathbf{4f^{12}5p^2}$, $4f^{11}5p^16s^2$, $4f^{11}5p^15d^2$, $4f^{11}5p^16p^2$, $4f^{11}5p^26s^1$, $4f^{11}5p^25d^1$, $4f^{11}5p^26p^1$, $4f^{12}5p^16s^1$, $4f^{12}5p^15d^1$, $4f^{12}5p^16p^1$	24,773	43,159,096	34,428,174
Ta V	$\mathbf{4f^{14}5p^65d^1}$, $4f^{13}5p^66s^2$, $4f^{13}5p^66d^2$, $4f^{13}5p^66p^2$, $4f^{14}5p^56s^2$, $4f^{14}5p^56d^2$, $4f^{14}5p^56p^2$, $4f^{14}5p^66s^1$, $4f^{14}5p^66d^1$, $4f^{14}5p^66p^1$	188	503	8
Ta VI	$\mathbf{4f^{14}}$, $4f^{12}6s^2$, $4f^{12}6d^2$, $4f^{12}6p^2$, $4f^{12}5d^16s^1$, $4f^{12}5d^16d^1$, $4f^{12}5d^16p^1$, $4f^{13}6s^1$, $4f^{13}6d^1$, $4f^{13}6p^1$	2510	446,729	2154
Ta VII	$\mathbf{4f^{13}5p^6}$, $4f^{11}5p^66s^2$, $4f^{11}5p^66d^2$, $4f^{11}5p^66p^2$, $4f^{12}5p^56s^2$, $4f^{12}5p^56d^2$, $4f^{12}5p^56p^2$, $4f^{13}5p^56s^1$, $4f^{13}5p^56d^1$, $4f^{13}5p^56p^1$	6119	323,087	6071
Ta VIII	$\mathbf{4f^{13}5p^5}$, $4f^{11}5p^56s^2$, $4f^{11}5p^56d^2$, $4f^{11}5p^56p^2$, $4f^{12}5p^46s^2$, $4f^{12}5p^46d^2$, $4f^{12}5p^46p^2$, $4f^{12}5p^56s^1$, $4f^{12}5p^56d^1$, $4f^{12}5p^56p^1$	23,497	6,130,471	140,369
Ta IX	$\mathbf{4f^{13}5p^4}$, $4f^{11}5p^46s^2$, $4f^{11}5p^46d^2$, $4f^{11}5p^46p^2$, $4f^{12}5p^36s^2$, $4f^{12}5p^36d^2$, $4f^{12}5p^36p^2$, $4f^{13}5p^36s^1$, $4f^{13}5p^36d^1$, $4f^{13}5p^36p^1$	44,996	7,220,318	72,766
Ta X	$\mathbf{4f^{13}5p^3}$, $4f^{11}5p^36s^2$, $4f^{11}5p^35d^2$, $4f^{11}5p^36p^2$, $4f^{12}5p^26s^2$, $4f^{12}5p^25d^2$, $4f^{12}5p^26p^2$, $4f^{13}5p^26s^1$, $4f^{13}5p^25d^1$, $4f^{13}5p^26p^1$	52,925	6,337,511	4,493,657
Ta XI	$\mathbf{4f^{13}5p^2}$, $4f^{11}5p^26s^2$, $4f^{11}5p^26d^2$, $4f^{11}5p^26p^2$, $4f^{12}5p^16s^2$, $4f^{12}5p^16d^2$, $4f^{12}5p^16p^2$, $4f^{13}5p^16s^1$, $4f^{13}5p^16d^1$, $4f^{13}5p^16p^1$	36,330	1,813,837	24,004
W V	$\mathbf{5d^2}$, $5d^16s^1$, $5d^16p^1$, $6s^16p^1$, $5d^15f^1$, $5d^17p^1$, $6s^17p^1$, $6p^17p^1$, $5d^17s^1$, $5d^16d^1$	97	1293	1243
WVI	$\mathbf{4f^{14}5d^1}$, $4f^{14}6s^1$, $4f^{14}6p^1$, $4f^{14}5f^1$, $4f^{14}6d^1$, $4f^{14}7s^1$, $4f^{14}5g^1$, $4f^{14}6g^1$, $4f^{14}7p^1$, $4f^{14}7d^1$	18	41	41
W VII	$\mathbf{4f^{14}}$, $4f^{13}6s^1$, $4f^{13}6p^1$, $4f^{13}5f^1$, $4f^{13}6d^1$, $4f^{13}7s^1$, $4f^{13}5g^1$, $4f^{13}6g^1$, $4f^{13}7p^1$, $4f^{13}7d^1$	155	2292	2292
W VIII	$\mathbf{4f^{13}5p^6}$, $4f^{14}5p^46s^1$, $4f^{14}5p^46p^1$, $4f^{14}5p^45f^1$, $4f^{14}5p^46d^1$, $4f^{14}5p^47s^1$, $4f^{14}5p^45g^1$, $4f^{14}5p^46g^1$, $4f^{14}5p^47p^1$, $4f^{14}5p^47d^1$	206	4994	4994
W IX	$\mathbf{4f^{14}5p^4}$, $4f^{14}5p^36s^1$, $4f^{14}5p^36p^1$, $4f^{14}5p^35f^1$, $4f^{14}5p^36d^1$, $4f^{14}5p^37s^1$, $4f^{14}5p^35g^1$, $4f^{14}5p^36g^1$, $4f^{14}5p^37p^1$, $4f^{14}5p^37d^1$	277	8568	8568
W X	$\mathbf{4f^{14}5p^3}$, $4f^{14}5p^26s^1$, $4f^{14}5p^26p^1$, $4f^{14}5p^25d^1$, $4f^{14}5p^16s^2$, $4f^{14}5p^16p^2$, $4f^{14}5p^15d^2$, $4f^{13}5p^26s^2$, $4f^{13}5p^26p^2$, $4f^{13}5p^25d^2$	1726	27,111	19,039
W XI	$\mathbf{4f^{14}5p^2}$, $4f^{13}5p^26s^1$, $4f^{13}5p^26p^1$, $4f^{13}5p^25f^1$, $4f^{13}5p^26d^1$, $4f^{13}5p^27s^1$, $4f^{13}5p^25g^1$, $4f^{13}5p^26g^1$, $4f^{13}5p^27p^1$, $4f^{13}5p^27d^1$	2183	418,768	418,768
Re V	$\mathbf{5d^3}$, $5d^26s^1$, $5d^26p^1$, $6s^26p^1$, $5d^25f^1$, $5d^27p^1$, $6s^27p^1$, $6p^27p^1$, $5d^27s^1$, $5d^26d^1$	314	11,621	10,148
Re VI	$\mathbf{5d^2}$, $5d^16s^1$, $5d^16p^1$, $6s^16p^1$, $5d^15f^1$, $5d^17p^1$, $6s^17p^1$, $6p^17p^1$, $5d^17s^1$, $5d^16d^1$	97	1293	1181
Re VII	$\mathbf{4f^{14}5d^1}$, $4f^{14}6s^1$, $4f^{14}6p^1$, $4f^{14}5f^1$, $4f^{14}6d^1$, $4f^{14}7s^1$, $4f^{14}5g^1$, $4f^{14}6g^1$, $4f^{14}7p^1$, $4f^{14}7d^1$	18	41	41
Re VIII	$\mathbf{4f^{14}5p^6}$, $4f^{14}5p^56s^1$, $4f^{14}5p^56p^1$, $4f^{14}5p^55f^1$, $4f^{14}5p^56d^1$, $4f^{14}5p^57s^1$, $4f^{14}5p^55g^1$, $4f^{14}5p^56g^1$, $4f^{14}5p^57p^1$, $4f^{14}5p^57d^1$	89	896	896
Re IX	$\mathbf{4f^{14}5p^5}$, $4f^{14}5p^46s^1$, $4f^{14}5p^46p^1$, $4f^{14}5p^45f^1$, $4f^{14}5p^46d^1$, $4f^{14}5p^47s^1$, $4f^{14}5p^45g^1$, $4f^{14}5p^46g^1$, $4f^{14}5p^47p^1$, $4f^{14}5p^47d^1$	206	4950	4950
Re X	$\mathbf{4f^{14}5p^4}$, $4f^{14}5p^36s^1$, $4f^{14}5p^36p^1$, $4f^{14}5p^35f^1$, $4f^{14}5p^36d^1$, $4f^{14}5p^37s^1$, $4f^{14}5p^35g^1$, $4f^{14}5p^36g^1$, $4f^{14}5p^37p^1$, $4f^{14}5p^37d^1$	277	8568	8568
Re XI	$\mathbf{4f^{14}5p^3}$, $4f^{14}5p^26s^1$, $4f^{14}5p^26p^1$, $4f^{14}5p^25f^1$, $4f^{14}5p^26d^1$, $4f^{14}5p^27s^1$, $4f^{14}5p^25g^1$, $4f^{14}5p^26g^1$, $4f^{14}5p^27p^1$, $4f^{14}5p^27d^1$	209	5176	5176
Os V	$\mathbf{5d^4}$, $5d^36s^1$, $5d^36p^1$, $5d^16s^26p^1$, $5d^26s^16p^1$, $5d^16s^16p^2$, $5d^35f^1$, $5d^37p^1$, $5d^27p^2$, $5d^16p^27p^1$, $5d^37s^1$, $5d^36d^1$	1131	143,017	70,770
Os VI	$\mathbf{5d^3}$, $5d^26s^1$, $5d^26p^1$, $5d^16s^16p^1$, $5d^25f^1$, $5d^27p^1$, $5d^17p^2$, $5d^16p^17p^1$, $5d^27s^1$, $5d^26d^1$	405	21,187	14,055
Os VII	$\mathbf{5d^2}$, $5d^16s^1$, $5d^16p^1$, $6s^16p^1$, $5d^15f^1$, $5d^17p^1$, $6s^17p^1$, $6p^17p^1$, $5d^17s^1$, $5d^16d^1$	97	1293	1243
Os VIII	$\mathbf{4f^{14}5d^1}$, $4f^{14}6s^1$, $4f^{14}6p^1$, $4f^{14}5f^1$, $4f^{14}6d^1$, $4f^{14}7s^1$, $4f^{14}5g^1$, $4f^{14}6g^1$, $4f^{14}7p^1$, $4f^{14}7d^1$	18	41	41
Os IX	$\mathbf{4f^{14}5p^6}$, $4f^{14}5p^56s^1$, $4f^{14}5p^56p^1$, $4f^{14}5p^55f^1$, $4f^{14}5p^56d^1$, $4f^{14}5p^57s^1$, $4f^{14}5p^55g^1$, $4f^{14}5p^56g^1$, $4f^{14}5p^57p^1$, $4f^{14}5p^57d^1$	89	896	896
Os X	$\mathbf{4f^{14}5p^5}$, $4f^{14}5p^46s^1$, $4f^{14}5p^46p^1$, $4f^{14}5p^45f^1$, $4f^{14}5p^46d^1$, $4f^{14}5p^47s^1$, $4f^{14}5p^45g^1$, $4f^{14}5p^46g^1$, $4f^{14}5p^47p^1$, $4f^{14}5p^47d^1$	206	4950	4950
Os XI	$\mathbf{4f^{14}5p^4}$, $4f^{14}5p^36s^1$, $4f^{14}5p^36p^1$, $4f^{14}5p^35f^1$, $4f^{14}5p^36d^1$, $4f^{14}5p^37s^1$, $4f^{14}5p^35g^1$, $4f^{14}5p^36g^1$, $4f^{14}5p^37p^1$, $4f^{14}5p^37d^1$	277	8568	8568
Ir V	$\mathbf{5d^5}$, $5d^36s^2$, $5d^46s^1$, $5d^36s^16p^1$, $5d^26s^26p^1$, $5d^46p^1$, $5d^36s^17s^1$, $5d^36s^18s^1$	705	58,122	43,221
Ir VI	$\mathbf{5d^4}$, $5d^26s^2$, $5d^26s^16p^1$, $5d^36s^1$	171	3606	3606
Ir VII	$\mathbf{5d^3}$, $5d^16s^2$, $6s^26p^1$, $5d^16s^16p^1$, $5d^26s^1$, $6s^27s^1$, $6s^27p^1$, $6s^26d^1$, $5d^16s^16p^2$, $6s^28s^1$, $6s^25f^1$, $6s^27d^1$, $6s^28p^1$, $5d^16s^17s^1$	90	1156	896
Ir VIII	$\mathbf{5d^2}$, $5d^16s^1$, $5d^16p^1$, $6s^16p^1$, $5d^15f^1$, $5d^17p^1$, $6s^17p^1$, $6p^17p^1$, $5d^17s^1$, $5d^16d^1$	97	1293	1280
Ir IX	$\mathbf{4f^{14}5d^1}$, $4f^{14}6s^1$, $4f^{14}6p^1$, $4f^{14}5f^1$, $4f^{14}6d^1$, $4f^{14}7s^1$, $4f^{14}5g^1$, $4f^{14}6g^1$, $4f^{14}7p^1$, $4f^{14}7d^1$	18	41	41
Ir X	$\mathbf{4f^{14}5p^6}$, $4f^{14}5p^56s^1$, $4f^{14}5p^56p^1$, $4f^{14}5p^55f^1$, $4f^{14}5p^56d^1$, $4f^{14}5p^57s^1$, $4f^{14}5p^55g^1$, $4f^{14}5p^56g^1$, $4f^{14}5p^57p^1$, $4f^{14}5p^57d^1$	89	896	896

Table B1
(Continued)

Ion	Configurations	N_{level}	N_{line}	N_{line}^*
Ir XI	$\mathbf{4f^{14}5p^5}$, $4f^{14}5p^46s^1$, $4f^{14}5p^46p^1$, $4f^{14}5p^45f^1$, $4f^{14}5p^46d^1$, $4f^{14}5p^47s^1$, $4f^{14}5p^45g^1$, $4f^{14}5p^46g^1$, $4f^{14}5p^47p^1$, $4f^{14}5p^47d^1$	206	4950	4950
Pt V	$\mathbf{5d^6}$, $5d^56s^1$, $5d^56p^1$, $5d^46s^2$, $5d^46s^16p^1$, $5d^46s^17s^1$	842	70,268	65,327
Pt VI	$\mathbf{5d^5}$, $5d^46s^1$, $5d^46p^1$, $5d^36s^2$, $5d^36s^16p^1$, $5d^26s^26p^1$, $5d^36s^17s^1$, $5d^36s^18s^1$	705	58,122	42,946
Pt VII	$\mathbf{5d^4}$, $5d^36s^1$, $5d^36p^1$, $5d^26s^2$, $5d^26s^16p^1$	281	7872	7872
Pt VIII	$\mathbf{5d^3}$, $5d^26s^1$, $5d^26p^1$, $5d^16s^2$, $6s^26p^1$, $5d^16s^16p^1$, $6s^27s^1$, $6s^27p^1$, $6s^26d^1$, $6s^16p^2$, $6s^28s^1$, $6s^25f^1$, $6s^27d^1$, $6s^28p^1$, $5d^16s^17s^1$	135	2666	2250
Pt IX	$\mathbf{5d^2}$, $6s^2$, $6s^16p^1$, $5d^16s^1$, $6s^17s^1$, $6s^17p^1$, $6s^16d^1$, $6s^18s^1$, $6p^2$, $6s^15f^1$, $6s^18p^1$, $6s^17d^1$, $6s^19s^1$, $6s^16f^1$, $6s^19p^1$, $6s^18d^1$	61	520	404
Pt X	$\mathbf{4f^{14}5d^1}$, $4f^{13}6s^2$, $4f^{12}5d^16s^2$, $4f^{13}6s^16p^1$, $4f^{13}5d^16s^1$, $4f^{12}6s^26p^1$, $4f^{13}6s^17s^1$, $4f^{13}6s^17p^1$, $4f^{13}5d^16p^1$, $4f^{13}6s^16d^1$, $4f^{13}6s^18s^1$, $4f^{13}6p^2$, $4f^{13}6s^18p^1$	489	26,962	2113
Pt XI	$\mathbf{4f^{14}5p^6}$, $4f^{12}5p^66s^2$, $4f^{13}5p^65d^1$, $4f^{13}5p^66p^1$, $4f^{13}5p^66s^1$, $4f^{12}5p^65d^16s^1$, $4f^{11}5p^65d^26s^1$, $4f^{13}5p^65d^16p^1$, $4f^{12}5p^66s^17s^1$, $4f^{12}5p^66s^16d^1$, $4f^{12}5p^66s^18s^1$, $4f^{11}5p^65d^16s^17s^1$	5974	1,055,973	169
Au V	$\mathbf{5d^7}$, $5d^56s^2$, $5d^66s^1$, $5d^56s^16p^1$, $5d^46s^26p^1$, $5d^56s^17s^1$, $5d^66p^1$, $5d^56s^16d^1$, $5d^56s^18s^1$, $5d^46s^27s^1$	1894	396,564	266,496
Au VI	$\mathbf{5d^6}$, $5d^46s^2$, $5d^56s^1$, $5d^46s^16p^1$, $5d^56p^1$, $5d^46s^17s^1$	842	70,268	68,707
Au VII	$\mathbf{5d^5}$, $5d^36s^2$, $5d^46s^1$, $5d^36s^16p^1$, $5d^26s^26p^1$, $5d^46p^1$, $5d^36s^17s^1$, $5d^36s^18s^1$	705	58,122	43,338
Au VIII	$\mathbf{5d^4}$, $5d^26s^2$, $5d^26s^16p^1$, $5d^36s^1$	171	3606	3606
Au IX	$\mathbf{5d^3}$, $5d^16s^2$, $6s^26p^1$, $5d^16s^16p^1$, $5d^26s^1$, $6s^27s^1$, $6s^27p^1$, $6s^26d^1$, $6s^16p^2$, $6s^28s^1$, $6s^25f^1$, $6s^27d^1$, $6s^28p^1$, $5d^16s^17s^1$	90	1156	896
Au X	$\mathbf{5d^2}$, $6s^2$, $6s^16p^1$, $5d^16s^1$, $6s^17s^1$, $6s^17p^1$, $6s^16d^1$, $6s^18s^1$, $6p^2$, $6s^15f^1$, $6s^18p^1$, $6s^17d^1$, $6s^19s^1$, $6s^16f^1$, $6s^19p^1$, $6s^18d^1$	61	520	378
Au XI	$\mathbf{4f^{14}5d^1}$, $4f^{13}6s^2$, $4f^{12}5d^16s^2$, $4f^{13}6s^16p^1$, $4f^{13}5d^16s^1$, $4f^{12}6s^26p^1$, $4f^{12}5d^16s^16p^1$, $4f^{13}6s^17s^1$, $4f^{13}6s^17p^1$, $4f^{13}5d^16p^1$, $4f^{13}6s^16d^1$, $4f^{13}6s^18s^1$, $4f^{13}6p^2$, $4f^{13}6s^18p^1$, $4f^{13}6s^117p^1$, $4f^{13}6s^118p^1$, $4f^{13}6s^119p^1$, $4f^{13}6s^120p^1$, $4f^{13}6s^130p^1$, $4f^{13}6s^131p^1$	1862	266,914	2048
Hg V	$\mathbf{5d^8}$, $5d^66s^2$, $5d^76s^1$, $5d^66s^16p^1$, $5d^66s^17s^1$	567	34,122	30,074
Hg VI	$\mathbf{5d^7}$, $5d^56s^2$, $5d^66s^1$, $5d^56s^16p^1$, $5d^46s^26p^1$, $5d^56s^17s^1$, $5d^66p^1$, $5d^56s^16d^1$, $5d^56s^18s^1$, $5d^46s^27s^1$	1894	396,564	291,191
Hg VII	$\mathbf{5d^6}$, $5d^46s^2$, $5d^56s^1$, $5d^46s^16p^1$, $5d^56p^1$, $5d^46s^17s^1$	842	70,268	69,613
Hg VIII	$\mathbf{5d^5}$, $5d^36s^2$, $5d^46s^1$, $5d^36s^16p^1$, $5d^26s^26p^1$, $5d^46p^1$, $5d^36s^17s^1$, $5d^36s^18s^1$	705	58,122	43,338
Hg IX	$\mathbf{5d^4}$, $5d^26s^2$, $5d^26s^16p^1$, $5d^36s^1$	171	3606	3606
Hg X	$\mathbf{5d^3}$, $5d^16s^2$, $6s^26p^1$, $5d^16s^16p^1$, $5d^26s^1$, $6s^27s^1$, $6s^27p^1$, $6s^26d^1$, $6s^16p^2$, $6s^28s^1$, $6s^25f^1$, $6s^27d^1$, $6s^28p^1$, $5d^16s^17s^1$	90	1156	917
Hg XI	$\mathbf{4f^{14}5d^2}$, $4f^{14}6s^2$, $4f^{14}6s^16p^1$, $4f^{13}5d^16s^2$, $4f^{14}5d^16s^1$, $4f^{13}6s^26p^1$, $4f^{14}6s^17s^1$, $4f^{13}5d^26s^1$, $4f^{14}6s^17p^1$, $4f^{14}6s^16d^1$	222	2531	1237
Tl V	$\mathbf{5d^9}$, $5d^76s^2$, $5d^86s^1$, $5d^76s^16p^1$, $5d^76s^17s^1$	324	12,007	12,,007
Tl VI	$\mathbf{5d^8}$, $5d^66s^2$, $5d^76s^1$, $5d^66s^16p^1$, $5d^66s^17s^1$	567	34,122	32,137
Tl VII	$\mathbf{5d^7}$, $5d^56s^2$, $5d^66s^1$, $5d^56s^16p^1$, $5d^46s^26p^1$, $5d^56s^17s^1$, $5d^66p^1$, $5d^56s^16d^1$, $5d^56s^18s^1$, $5d^46s^27s^1$	1894	396,564	307,512
Tl VIII	$\mathbf{5d^6}$, $5d^46s^2$, $5d^56s^1$, $5d^46s^16p^1$, $5d^56p^1$, $5d^46s^17s^1$	842	70,268	70,268
Tl IX	$\mathbf{5d^5}$, $5d^36s^2$, $5d^46s^1$, $5d^36s^16p^1$, $5d^26s^26p^1$, $5d^46p^1$, $5d^36s^17s^1$, $5d^36s^18s^1$	705	58,122	44,037
Tl X	$\mathbf{5d^4}$, $5d^26s^2$, $5d^26s^16p^1$, $5d^36s^1$	171	3606	3606
Tl XI	$\mathbf{5d^3}$, $5d^16s^2$, $6s^26p^1$, $5d^16s^16p^1$, $5d^26s^1$, $6s^27s^1$, $6s^27p^1$, $6s^26d^1$, $6s^16p^2$, $6s^28s^1$, $6s^25f^1$, $6s^27d^1$, $6s^28p^1$, $5d^16s^17s^1$	90	1156	951
Pb V	$\mathbf{5d^{10}}$, $5d^96s^1$, $5d^96p^1$, $5d^96d^1$, $5d^97s^1$, $5d^97p^1$, $5d^97d^1$, $5d^86s^2$, $5d^86s^16p^1$, $5d^86s^17s^1$	182	4167	4000
Pb VI	$\mathbf{5d^9}$, $5d^76s^2$, $5d^86s^1$, $5d^76s^16p^1$, $5d^76s^17s^1$	324	12,007	11,055
Pb VII	$\mathbf{5d^8}$, $5d^66s^2$, $5d^76s^1$, $5d^66s^16p^1$, $5d^66s^17s^1$	567	34,122	33,915
Pb VIII	$\mathbf{5d^7}$, $5d^56s^2$, $5d^66s^1$, $5d^56s^16p^1$, $5d^46s^26p^1$, $5d^56s^17s^1$, $5d^66p^1$, $5d^56s^16d^1$, $5d^56s^18s^1$, $5d^46s^27s^1$	1894	396,564	325,532
Pb IX	$\mathbf{5d^6}$, $5d^46s^2$, $5d^56s^1$, $5d^46s^16p^1$, $5d^56p^1$, $5d^46s^17s^1$	842	70,268	70,268
Pb X	$\mathbf{5d^5}$, $5d^36s^2$, $5d^46s^1$, $5d^36s^16p^1$, $5d^26s^26p^1$, $5d^46p^1$, $5d^36s^17s^1$, $5d^36s^18s^1$	705	58,122	46,809
Pb XI	$\mathbf{5d^4}$, $5d^26s^2$, $5d^26s^16p^1$, $5d^36s^1$	171	3606	3606
Bi V	$\mathbf{5d^{10}6s^1}$, $5d^{10}6p^1$, $5d^96s^2$, $5d^{10}6d^1$, $5d^{10}7s^1$, $5d^{10}7p^1$, $5d^{10}7d^1$, $5d^{10}8s^1$, $5d^96s^16p^1$, $5d^{10}8p^1$	38	186	186
Bi VI	$\mathbf{5d^{10}}$, $5d^96s^1$, $5d^96p^1$, $5d^96d^1$, $5d^95f^1$, $5d^86s^16p^1$, $5d^97s^1$, $5d^97p^1$, $5d^96f^1$, $5d^86s^2$, $5d^86s^17s^1$	222	5461	5461
Bi VII	$\mathbf{5d^9}$, $5d^76s^2$, $5d^86s^1$, $5d^76s^16p^1$, $5d^76s^17s^1$	324	12,007	12,007
Bi VIII	$\mathbf{5d^8}$, $5d^66s^2$, $5d^76s^1$, $5d^66s^16p^1$, $5d^66s^17s^1$	567	34,122	34,122
Bi IX	$\mathbf{5d^7}$, $5d^56s^2$, $5d^66s^1$, $5d^56s^16p^1$, $5d^46s^26p^1$, $5d^56s^17s^1$, $5d^66p^1$, $5d^56s^16d^1$, $5d^56s^18s^1$, $5d^46s^27s^1$	1894	396,564	343,315
Bi X	$\mathbf{5d^6}$, $5d^46s^2$, $5d^56s^1$, $5d^46s^16p^1$, $5d^56p^1$, $5d^46s^17s^1$	842	70,268	70,268
Bi XI	$\mathbf{5d^5}$, $5d^36s^2$, $5d^46s^1$, $5d^36s^16p^1$, $5d^26s^26p^1$, $5d^46p^1$, $5d^36s^17s^1$, $5d^36s^18s^1$	705	58,122	47,199
Po V	$\mathbf{6s^2}$, $6s^16p^1$, $6s^17s^1$, $6s^17p^1$, $6s^16d^1$, $6s^18s^1$, $6s^18p^1$, $6s^17d^1$, $6s^15f^1$	29	130	130
Po VI	$\mathbf{5d^{10}6s^1}$, $5d^96s^2$, $5d^{10}6p^1$, $5d^96s^16p^1$, $5d^{10}7s^1$, $5d^{10}7p^1$, $5d^{10}6d^1$, $5d^{10}8s^1$, $5d^{10}8p^1$, $5d^{10}6s^1$	36	141	141
Po VII	$\mathbf{5d^{10}}$, $5d^96s^1$, $5d^86s^2$, $5d^86s^16p^1$, $5d^96p^1$, $5d^97s^1$, $5d^86s^17s^1$	152	2729	2729
Po VIII	$\mathbf{5d^9}$, $5d^76s^2$, $5d^86s^1$, $5d^76s^16p^1$, $5d^76s^17s^1$	324	12,007	12,007
Po IX	$\mathbf{5d^8}$, $5d^66s^2$, $5d^76s^1$, $5d^66s^16p^1$, $5d^66s^17s^1$	567	34,122	34,122

Table B1
(Continued)

Ion	Configurations	N_{level}	N_{line}	N_{line}^*
Po X	$\mathbf{5d^7}$, $5d^56s^2$, $5d^66s^1$, $5d^56s^16p^1$, $5d^46s^26p^1$, $5d^56s^17s^1$, $5d^66p^1$, $5d^56s^16d^1$, $5d^56s^18s^1$, $5d^46s^27s^1$	1894	396,564	332,014
Po XI	$\mathbf{5d^6}$, $5d^46s^2$, $5d^56s^1$, $5d^46s^16p^1$, $5d^56p^1$, $5d^46s^17s^1$	842	70,268	70,268
At V	$\mathbf{6s^2}6p^1$, $6s^27s^1$, $6s^27p^1$, $6s^26d^1$, $6s^28s^1$, $6s^28p^1$, $6s^27d^1$, $6s^25f^1$, $6s^16p^2$	22	85	85
At VI	$\mathbf{6s^2}$, $6s^16p^1$, $6s^16d^1$, $6s^17p^1$	13	26	26
At VII	$\mathbf{5d^{10}}6s^1$, $5d^96s^2$, $5d^{10}6p^1$, $5d^{10}7s^1$, $5d^{10}7p^1$, $5d^{10}6d^1$, $5d^{10}8s^1$, $5d^{10}8p^1$, $5d^{10}6s^1$	13	36	36
At VIII	$\mathbf{5d^{10}}$, $5d^96s^1$, $5d^86s^2$, $5d^86s^16p^1$, $5d^96p^1$, $5d^97s^1$, $5d^86s^17s^1$	152	2729	2729
At IX	$\mathbf{5d^9}$, $5d^76s^2$, $5d^86s^1$, $5d^76s^16p^1$, $5d^76s^17s^1$	324	12,007	12,007
At X	$\mathbf{5d^8}$, $5d^66s^2$, $5d^76s^1$, $5d^66s^16p^1$, $5d^66s^17s^1$	567	34,122	34,122
At XI	$\mathbf{5d^7}$, $5d^56s^2$, $5d^66s^1$, $5d^56s^16p^1$, $5d^46s^26p^1$, $5d^56s^17s^1$, $5d^66p^1$, $5d^56s^16d^1$, $5d^56s^18s^1$, $5d^46s^27s^1$	1894	396,564	337,686
Rn V	$\mathbf{6p^2}$, $6p^17s^1$, $6p^17p^1$, $6p^16d^1$, $6p^18s^1$, $6p^18p^1$, $6p^17d^1$, $6p^15f^1$, $6p^19s^1$, $6p^19p^1$, $6p^18d^1$	95	1398	43
Rn VI	$\mathbf{6s^2}6p^1$, $6s^27s^1$, $6s^27p^1$, $6s^26d^1$, $6s^28s^1$, $6s^28p^1$, $6s^27d^1$, $6s^25f^1$, $6s^16p^2$	22	85	85
Rn VII	$\mathbf{6s^2}$, $6s^16p^1$, $\mathbf{6s^1}7s^1$, $6s^17p^1$, $6s^16d^1$, $6s^18s^1$, $6s^18p^1$, $6s^17d^1$, $6s^15f^1$, $6s^16f^1$	33	152	152
Rn VIII	$\mathbf{5d^{10}}6s^1$, $5d^96s^2$, $5d^{10}6p^1$, $5d^96s^16p^1$, $5d^{10}7s^1$, $5d^{10}7p^1$, $5d^{10}6d^1$, $5d^{10}8s^1$, $5d^{10}8p^1$	36	141	141
Rn IX	$\mathbf{5d^{10}}$, $5d^96s^1$, $5d^86s^2$, $5d^86s^16p^1$, $5d^96p^1$, $5d^97s^1$, $5d^86s^17s^1$	152	2729	2729
Rn X	$\mathbf{5d^9}$, $5d^76s^2$, $5d^86s^1$, $5d^76s^16p^1$, $5d^76s^17s^1$	324	12,007	12,007
Rn XI	$\mathbf{5d^8}$, $5d^66s^2$, $5d^76s^1$, $5d^66s^16p^1$, $5d^66s^17s^1$	567	34,122	34,122
Fr V	$\mathbf{6p^3}$, $6p^27s^1$, $6p^27p^1$, $6p^26d^1$, $6p^28s^1$, $6p^28p^1$, $6p^27d^1$, $6p^29s^1$, $6p^29p^1$, $6p^28d^1$	176	4986	2656
Fr VI	$\mathbf{6p^2}$, $6p^17s^1$, $6p^17p^1$, $6p^16d^1$, $6p^18s^1$, $6p^18p^1$, $6p^17d^1$, $6p^15f^1$, $6p^19s^1$, $6p^19p^1$, $6p^18d^1$	95	1398	1398
Fr VII	$\mathbf{6s^2}6p^1$, $6s^16p^2$, $6s^27s^1$, $6s^27p^1$, $6s^26d^1$, $6s^28s^1$, $6s^28p^1$, $6s^27d^1$, $6s^25f^1$	22	85	0
Fr VIII	$\mathbf{5d^{10}}6s^2$, $5d^{10}6s^2$, $5d^{10}6s^16p^1$, $5d^{10}6s^17s^1$, $5d^96s^26p^1$, $5d^{10}6s^17p^1$, $5d^{10}6s^16d^1$, $5d^{10}6s^18s^1$, $5d^{10}6s^18p^1$, $5d^{10}6s^17d^1$, $5d^{10}6s^15f^1$	41	229	229
Fr IX	$\mathbf{5d^{10}}6s^1$, $5d^96s^2$, $5d^{10}6p^1$, $5d^96s^16p^1$, $5d^{10}7s^1$, $5d^{10}7p^1$, $5d^{10}6d^1$, $5d^{10}8s^1$, $5d^{10}8p^1$, $5d^{10}6s^1$	36	141	5
Fr X	$\mathbf{5d^{10}}$, $5d^96s^1$, $5d^86s^2$, $5d^86s^16p^1$, $5d^96p^1$, $5d^97s^1$, $5d^86s^17s^1$	152	2729	2729
Fr XI	$\mathbf{5d^9}$, $5d^76s^2$, $5d^86s^1$, $5d^76s^16p^1$, $5d^76s^17s^1$	324	12,007	12,007
Ra V	$\mathbf{6p^4}$, $6p^37s^1$, $6p^37p^1$, $6p^36d^1$, $6p^38s^1$, $6p^38p^1$, $6p^37d^1$, $6p^39s^1$, $6p^38d^1$, $6p^310p^1$	251	9553	4793
Ra VI	$\mathbf{6p^3}$, $6p^27s^1$, $6p^27p^1$, $6p^26d^1$, $6p^28s^1$, $6p^28p^1$, $6p^27d^1$, $6p^29s^1$, $6p^29p^1$, $6p^28d^1$	176	4986	3201
Ra VII	$\mathbf{6p^2}$, $6p^17s^1$, $6p^17p^1$, $6p^16d^1$, $6p^18s^1$, $6p^18p^1$, $6p^17d^1$, $6p^15f^1$, $6p^19s^1$, $6p^19p^1$, $6p^18d^1$	95	1398	1398
Ra VIII	$\mathbf{6s^2}6p^1$, $6s^16p^2$, $6s^27s^1$, $6s^27p^1$, $6s^26d^1$, $6s^28s^1$, $6s^28p^1$, $6s^27d^1$, $6s^25f^1$	22	85	85
Ra IX	$\mathbf{5d^{10}}6s^2$, $5d^{10}6s^2$, $5d^{10}6s^16p^1$, $5d^{10}6s^17s^1$, $5d^96s^26p^1$, $5d^{10}6s^17p^1$, $5d^{10}6s^16d^1$, $5d^{10}6s^18s^1$, $5d^{10}6s^18p^1$, $5d^{10}6s^17d^1$, $5d^{10}6s^15f^1$	41	229	229
Ra X	$\mathbf{5d^{10}}6s^1$, $5d^96s^2$, $5d^{10}6p^1$, $5d^96s^16p^1$, $5d^{10}7s^1$, $5d^{10}7p^1$, $5d^{10}6d^1$, $5d^{10}8s^1$, $5d^{10}8p^1$, $5d^{10}6s^1$	36	141	141
Ra XI	$\mathbf{5d^{10}}$, $5d^96s^1$, $5d^86s^2$, $5d^86s^16p^1$, $5d^96p^1$, $5d^97s^1$, $5d^86s^17s^1$	152	2729	2729

Note. N_{level}, N_{line}, and N_{line}^* represent the number of energy levels, transitions involving all the energy levels, and the transitions involving the energy levels below the ionization threshold, respectively.

(This table is available in machine-readable form.)

ORCID iDs

Smaranika Banerjee https://orcid.org/0000-0002-0786-7307
Masaomi Tanaka https://orcid.org/0000-0001-8253-6850
Daiji Kato https://orcid.org/0000-0002-5302-073X
Gediminas Gaigalas https://orcid.org/0000-0003-0039-1163

References

Abbott, B. P., Abbott, R., Abbott, T. D., et al. 2017, PhRvL, 119, 161101
Arcavi, I. 2018, ApJL, 855, L23
Banerjee, S., Tanaka, M., Kato, D., et al. 2022, ApJ, 934, 117
Banerjee, S., Tanaka, M., Kawaguchi, K., Kato, D., & Gaigalas, G. 2020, ApJ, 901, 29
Barnes, J., Kasen, D., Wu, M.-R., & Martínez-Pinedo, G. 2016, ApJ, 829, 110
Bar-Shalom, A., Klapisch, M., & Oreg, J. 2001, JQSRT, 71, 169
Bauswein, A., Goriely, S., & Janka, H. T. 2013, ApJ, 773, 78
Carlson, T. A., Nestor, C., Wasserman, N., & Mcdowell, J. 1970, ADNDT, 2, 63
Carvajal Gallego, H., Berengut, J. C., Palmeri, P., & Quinet, P. 2022a, MNRAS, 509, 6138
Carvajal Gallego, H., Berengut, J. C., Palmeri, P., & Quinet, P. 2022b, MNRAS, 513, 2302
Carvajal Gallego, H., Deprince, J., Berengut, J. C., Palmeri, P., & Quinet, P. 2023, MNRAS, 518, 332
Carvajal Gallego, H., Deprince, J., Godefroid, M., et al. 2023, EPJD, 77, 72
Chase, E. A., O'Connor, B., Fryer, C. L., et al. 2022, ApJ, 927, 163
Colombo, A., Salafia, O. S., Gabrielli, F., et al. 2022, ApJ, 937, 79
Combi, L., & Siegel, D. M. 2023, ApJ, 944, 28
Coulter, D. A., Foley, R. J., Kilpatrick, C. D., et al. 2017, Sci, 358, 1556
Cowan, R. D. 1967, PhRv, 163, 54
Cowan, R. D. 1973, NucIM, 110, 173
Cowan, R. D. 1981, The Theory of Atomic Structure and Spectra (Los Alamos Series in Basic and Applied Sciences) (Berkeley, CA: Univ. California Press)
Cowperthwaite, P. S., Berger, E., Villar, V. A., et al. 2017, ApJL, 848, L17
Dekany, R., Smith, R. M., Riddle, R., et al. 2020, PASP, 132, 038001
Dorsman, B., Raaijmakers, G., Cenko, S. B., et al. 2023, ApJ, 944, 126
Drout, M. R., Piro, A. L., Shappee, B. J., et al. 2017, Sci, 358, 1570
Eastman, R. G., & Pinto, P. A. 1993, ApJ, 412, 731
Eichler, D., Livio, M., Piran, T., & Schramm, D. N. 1989, Natur, 340, 126
Fernandez, R., & Metzger, B. 2014, AAS/HEAD Meeting, 14, 304
Flörs, A., Silva, R. F., Deprince, J., et al. 2023, MNRAS, 524, 3083
Fontes, C. J., Fryer, C. L., Hungerford, A. L., Wollaeger, R. T., & Korobkin, O. 2020, MNRAS, 493, 4143
Fontes, C. J., Fryer, C. L., Hungerford, A. L., et al. 2015, HEDP, 16, 53

Fontes, C. J., Fryer, C. L., Wollaeger, R. T., Mumpower, M. R., & Sprouse, T. M. 2023, MNRAS, 519, 2862

Freiburghaus, C., Rosswog, S., & Thielemann, F. K. 1999, ApJL, 525, L121

Fujibayashi, S., Kiuchi, K., Nishimura, N., Sekiguchi, Y., & Shibata, M. 2018, ApJ, 860, 64

Fujibayashi, S., Kiuchi, K., Wanajo, S., et al. 2023, ApJ, 942, 39

Fujibayashi, S., Shibata, M., Wanajo, S., et al. 2020a, PhRvD, 101, 083029

Fujibayashi, S., Wanajo, S., Kiuchi, K., et al. 2020b, ApJ, 901, 122

Gaigalas, G., Kato, D., Rynkun, P., Radžiūtė, L., & Tanaka, M. 2019, ApJS, 240, 29

Gottlieb, O., & Loeb, A. 2020, MNRAS, 493, 1753

Hamidani, H., & Ioka, K. 2023a, MNRAS, 524, 4841

Hamidani, H., & Ioka, K. 2023b, MNRAS, 520, 1111

Hamidani, H., Kimura, S. S., Tanaka, M., & Ioka, K. 2024, ApJ, 963, 137

Just, O., Bauswein, A., Ardevol Pulpillo, R., Goriely, S., & Janka, H. T. 2015, MNRAS, 448, 541

Just, O., Kullmann, I., Goriely, S., et al. 2022, MNRAS, 510, 2820

Karp, A. H., Lasher, G., Chan, K. L., & Salpeter, E. E. 1977, ApJ, 214, 161

Kasen, D., Badnell, N. R., & Barnes, J. 2013, ApJ, 774, 25

Kasen, D., Metzger, B., Barnes, J., Quataert, E., & Ramirez-Ruiz, E. 2017, Natur, 551, 80

Kasliwal, M. M., Nakar, E., Singer, L. P., et al. 2017, Sci, 358, 1559

Kawaguchi, K., Shibata, M., & Tanaka, M. 2018, ApJL, 865, L21

Kilbane, D., & O'Sullivan, G. 2010, PhRvA, 82, 062504

Klion, H., Duffell, P. C., Kasen, D., & Quataert, E. 2021, MNRAS, 502, 865

Korobkin, O., Rosswog, S., Arcones, A., & Winteler, C. 2012, MNRAS, 426, 1940

Kramida, A., Ralchenko, Yu., Reader, J. & NIST ASD Team 2020, NIST Atomic Spectra Database v5.8, National Institute of Standards and Technology, Gaithersburg, MD, https://physics.nist.gov/asd

Kulkarni, S. R. 2005, arXiv:astro-ph/0510256

Kulkarni, S. R., Harrison, F. A., Grefenstette, B. W., et al. 2021, arXiv:2111.15608

Lattimer, J. M., & Schramm, D. N. 1974, ApJL, 192, L145

Li, L.-X., & Paczyński, B. 1998, ApJL, 507, L59

Lippuner, J., Fernández, R., Roberts, L. F., et al. 2017, MNRAS, 472, 904

Maison, L., Carvajal Gallego, H., & Quinet, P. 2022, Atoms, 10, 130

Martin, W. C., Zalubas, R., & Hagan, L. 1978, Atomic Energy Levels - The Rare Earth Elements NSRDS-NBS 60, National Bureau of Standards, U.S. Department of Commerce

Metzger, B. D., Bauswein, A., Goriely, S., & Kasen, D. 2015, MNRAS, 446, 1115

Metzger, B. D., & Fernández, R. 2014, MNRAS, 441, 3444

Metzger, B. D., Martínez-Pinedo, G., Darbha, S., et al. 2010, MNRAS, 406, 2650

Metzger, B. D., Piro, A. L., & Quataert, E. 2008, MNRAS, 390, 781

Metzger, B. D., Thompson, T. A., & Quataert, E. 2018, ApJ, 856, 101

Miller, J. M., Ryan, B. R., Dolence, J. C., et al. 2019, PhRvD, 100, 023008

Ohgami, T., Becerra Gonzalez, J., Tominaga, N., et al. 2023, ApJ, 947, 9

Ohgami, T., Tominaga, N., Utsumi, Y., et al. 2021, PASJ, 73, 350

Perego, A., Radice, D., & Bernuzzi, S. 2017, ApJL, 850, L37

Perego, A., Rosswog, S., Cabezón, R. M., et al. 2014, MNRAS, 443, 3134

Piro, A. L., & Kollmeier, J. A. 2018, ApJ, 855, 103

Rodrigues, G. C., Indelicato, P., Santos, J. P., Patté, P., & Parente, F. 2004, ADNDT, 86, 117

Roming, P. W. A., Kennedy, T. E., Mason, K. O., et al. 2005, SSRv, 120, 95

Rosswog, S., Sollerman, J., Feindt, U., et al. 2018, A&A, 615, A132

Rynkun, P., Banerjee, S., Gaigalas, G., et al. 2022, A&A, 658, A82

Sagiv, I., Gal-Yam, A., Ofek, E. O., et al. 2014, AJ, 147, 79

Sekiguchi, Y., Kiuchi, K., Kyutoku, K., & Shibata, M. 2015, PhRvD, 91, 064059

Shibata, M., Fujibayashi, S., Hotokezaka, K., et al. 2017, PhRvD, 96, 123012

Shibata, M., & Hotokezaka, K. 2019, ARNPS, 69, 41

Smartt, S. J., Chen, T. W., Jerkstrand, A., et al. 2017, Natur, 551, 75

Sobolev, V. V. 1960, SvA, 4, 372

Sugar, J., & Kaufman, V. 1975, PhRvA, 12, 994

Tanaka, M., & Hotokezaka, K. 2013, ApJ, 775, 113

Tanaka, M., Kato, D., Gaigalas, G., & Kawaguchi, K. 2020, MNRAS, 496, 1369

Tanaka, M., Kato, D., Gaigalas, G., et al. 2018, ApJ, 852, 109

Tanaka, M., Utsumi, Y., Mazzali, P. A., et al. 2017, PASJ, 69, 102

Utsumi, Y., Tanaka, M., Tominaga, N., Yoshida, M., et al. 2017, PASJ, 69, 101

Valenti, S., Sand, D. J., Yang, S., et al. 2017, ApJL, 848, L24

Villar, V. A., Guillochon, J., Berger, E., et al. 2017, ApJL, 851, L21

Wanajo, S., Sekiguchi, Y., Nishimura, N., et al. 2014, ApJL, 789, L39

Waxman, E., Ofek, E. O., Kushnir, D., & Gal-Yam, A. 2018, MNRAS, 481, 3423

Wollaeger, R. T., Hungerford, A. L., Fryer, C. L., et al. 2017, ApJ, 845, 168

Yang, S., Valenti, S., Cappellaro, E., et al. 2017, ApJL, 851, L48

Yu, Y.-W., Zhang, B., & Gao, H. 2013, ApJL, 776, L40